



Key Points:

- A new cost-efficient approach is developed for modeling gas dissolution effect in Eulerian-Eulerian LES
- The new LES model to simulate the hydrocarbon plumes in deep-water environment
- Results suggest that omitting gas dissolution may cause overestimation of peel and intrusion heights by up to 151% and 127%

Correspondence to:

D. Yang,
diyang@uh.edu

Citation:

Peng, C., Xiao, S., & Yang, D. (2020). Large-eddy simulation model for the effect of gas bubble dissolution on the dynamics of hydrocarbon plume from deep-water blowout. *Journal of Geophysical Research: Oceans*, 125, e2019JC016037. <https://doi.org/10.1029/2019JC016037>

Received 30 DEC 2019

Accepted 13 MAY 2020

Accepted article online 22 MAY 2020

Large-Eddy Simulation Model for the Effect of Gas Bubble Dissolution on the Dynamics of Hydrocarbon Plume from Deep-Water Blowout

Chen Peng¹ , Shuolin Xiao¹ , and Di Yang¹

¹Department of Mechanical Engineering, University of Houston, Houston, TX, USA

Abstract During a deep-water wellhead blowout incident, the dynamics of the released hydrocarbon plume is strongly affected by the gas dissolution process that weakens the bubble-induced buoyancy for driving the plume. In this study, a new modeling strategy is developed to efficiently incorporate the gas dissolution effect into a fast Eulerian-Eulerian large-eddy simulation (LES) model. By simultaneously simulating the evolutions of the bubble mass concentration and number density functions, the average bubble size in each LES computational cell can be calculated locally. Based on the cell-averaged bubble diameter, the local gas dissolution rate and bubble rise velocity are parameterized, which are then used in the gas transport equations to model the evolution of the gas bubble field due to turbulent transport and gas dissolution. This LES model is applied to simulate several blowout scenarios with different initial bubble sizes. The results show that the plumes that have smaller initial bubble size exhibit faster relative bubble dissolution rate compared to the plumes with larger initial bubble size. As a result, the plumes with smaller bubbles also have lower peel and trap heights than those with larger bubbles. For comparison, a second set of LES runs with identical conditions but without including the gas dissolution effect are also performed. The data analysis shows that the omission of gas dissolution can cause overestimations of the plume peel and trap heights for up to 151% and 127%, respectively, suggesting the importance of including the gas dissolution effect for accurately modeling the near-field hydrocarbon plumes.

1. Introduction

The hydrocarbon plume released from a deep-water wellhead blowout is typically formed by a mixture of gas bubbles and oil droplets (McNutt et al., 2012; Reddy et al., 2012; Yapa & Zheng, 1997). After being released from the wellhead, the initial flow momentum is quickly dissipated over a relatively small distance (Camilli et al., 2012), and the gas and oil quickly break up into a large number of bubbles (Zhao et al., 2016a) and droplets (Zhao et al., 2016b), respectively. The multiphase hydrocarbon flow then continues to rise as a turbulent plume driven primarily by the buoyancy force induced by the gas bubbles and interacts with the stably stratified seawater in a highly dynamic manner (Gros et al., 2017; Socolofsky et al., 2011). In the case of a deep-water blowout, the gas bubbles can have sufficient time to interact with the surrounding seawater when rising through the ocean column. When rising toward higher elevation, two processes occur simultaneously and induce opposite effects (Dissanayake et al., 2018; Zheng & Yapa, 2002): (i) the bubbles expand while rising due to the decrease of hydrostatic pressure; (ii) the gas dissolution from the bubbles into the surrounding seawater causes the bubbles to shrink, which can significantly reduce the bubble-induced buoyancy for driving the plume. The combined effect of these two processes and the seawater stratification govern the dynamics of the near-field plume from a deep-water wellhead blowout.

Accurately quantifying the gas dissolution rate and its effect on the characteristics of the plume structure and material transport in a deep-water wellhead blowout is a difficult task. This is largely due to the technical challenges for measuring the detailed information inside the multiphase hydrocarbon plume in the deep-water environment (McNutt et al., 2012). To help understand the effect of bubbles on the plume dynamics, some studies have focused on measuring the flow and bubble dynamics in simple bubble-driven plumes in laboratory experiments (e.g., Lai & Socolofsky, 2019; Seol et al., 2009; Wang et al., 2019; Wang & Socolofsky, 2019). In order to achieve fast prediction of the near-field plume dynamics, many previous studies have devoted considerable efforts to developing and improving the one-dimensional integral plume

modeling approach (e.g., Asaeda & Imberger, 1993; Crouse et al., 2007; Dissanayake et al., 2018; Socolofsky et al., 2008; Yapa & Li, 1997; Zheng & Yapa, 2002). These integral models calculate the plume-integrated physical quantities as a function of the height by solving a set of one-dimensional ordinary differential equations derived from the cross-plume integration of the three-dimensional Navier-Stokes equations and material transport equations. The low computational cost associated with these models have made them valuable tools for quick modeling to support the decision making for rapid response to subsea wellhead blowout accidents.

Several studies have attempted to include the gas dissolution effect in the integral plume modeling framework. For example, Zheng and Yapa (2002) included the methane bubble dissolution effect in the integral plume model by modeling the mass transfer of methane based on empirical parameterizations of mass transfer coefficient and bubble rise velocity. Their integral model was able to capture the effect of the gas dissolution on the vertical variations of the mean inner plume characteristics, such as the reductions of bubble diameter, buoyancy flux, and momentum flux with the plume elevation. This model was further validated and upgraded with additional features added to the model (Chen & Yapa, 2003; Yapa et al., 2010; Zheng et al., 2003). Dissanayake et al. (2018) incorporated dissolution of multicomponent gas bubbles (methane, ethane, propane, etc., all in one bubble) in both double-plume and Lagrangian plume integral models and successfully modeled the near-field plume dynamics under deep-water blowout conditions similar to those in the Deepwater Horizon accident.

In recent years, large-eddy simulation (LES) has become a powerful numerical tool for high-fidelity simulations of the turbulent flow physics in buoyant plumes (e.g., Chen et al., 2018; Deen et al., 2001; Dhotre et al., 2013; Fabregat et al., 2015; Fraga et al., 2016; Hu & Celik, 2008; Yang et al., 2014). LES can model the time evolution of the plume structures with a wide range of scales of turbulent flow motions being resolved (down to the computational grid scale). While it still requires the unresolved subgrid-scale (SGS) effects to be modeled, LES can directly capture the turbulent flow and material transport phenomena above the computational grid scale, which can provide detailed plume field information to help assess, calibrate, and improve the integral plume model (Fraga & Stoesser, 2016; Yang et al., 2016). To model the multiphase plume flow from a subsea blowout using LES, the seawater flow is typically modeled as a continuous phase carrier flow governed by the filtered Navier-Stokes equations, while the gas bubbles and oil droplets are modeled as dispersed phases that are transported by the turbulent carrier flow. There are two major approaches for modeling the dispersed phase transport, that is, the Lagrangian approach and the Eulerian approach (Sokolichin et al., 1997). In the Lagrangian approach, the motions of each individual particles are simulated based on Newton's second law (e.g., Fraga et al., 2016; Fraga & Stoesser, 2016; Hu & Celik, 2008). In the Eulerian approach, the spatial distribution of a dispersed particle phase is described using an Eulerian concentration function, and its time evolution is modeled by solving an advection-diffusion equation to model the transport of the dispersed particles by the turbulent plume flow (e.g. Chen et al., 2018; Fabregat et al., 2015; Fabregat Tomàs et al., 2016; Yang et al., 2016). In combination with the Eulerian approach for modeling the carrier flow, the former plume modeling approach is usually referred to as the Eulerian-Lagrangian approach, and the latter is referred to as the Eulerian-Eulerian approach.

While it may be straightforward to add additional equations in the Lagrangian approach to model the gas dissolution from individual bubbles to the surrounding seawater, the overall computational cost of the Eulerian-Lagrangian approach can be quite high when modeling the plume of a realistic-scale deep-water blowout event in which a huge number of Lagrangian particles need to be tracked simultaneously. Therefore, the application of the Eulerian-Lagrangian LES model has been mainly limited to the laboratory scale problem (e.g., Fraga et al., 2016; Fraga & Stoesser, 2016), in which the gas bubbles do not have sufficient time to dissolve mass into the water so that the gas dissolution effect is often not modeled. On the other hand, the Eulerian-Eulerian approach has been successfully applied to model plumes at realistic scales (e.g., Chen et al., 2018; Yang et al., 2015). Note that in a typical Eulerian-Eulerian model with polydisperse particles, the distribution of each particle species (e.g., gas bubbles within the same discretized diameter bin) need to be modeled by a separate Eulerian concentration function. As a result, if the bubbles in the plume from a deep-water blowout experience size reduction over a wide range of diameters due to gas dissolution, a large number of Eulerian concentration functions may need to be used to cover the diameter bins. For example, Liang et al. (2012) developed an Eulerian-Eulerian LES model based on the multiple-bin approach (e.g., 17 bins of bubble sizes in their reported results) and applied it to simulate the bubble distribution in the ocean surface layer and the effect of air bubble dissolution on the air-sea gas transfer.

This current study aims at developing a new cost-efficient approach to include the effect of gas bubble dissolution in the Eulerian-Eulerian LES model framework for deep-water hydrocarbon plumes. The basic turbulent flow and particle transport LES solver for modeling oceanic plumes is adopted from Yang et al. (2014, 2015), which has been successfully applied to simulate multiphase buoyant plumes at both laboratory scale (e.g., Yang et al., 2016) and field scale (e.g., Chen et al., 2018). In the current LES modeling approach, the evolutions of both the Eulerian mass concentration and bubble number density functions of the gas bubbles are simulated simultaneously, based on which the cell-averaged bubble equivalent diameter can be calculated. Then the cell-averaged gas mass transfer coefficient and bubble rise velocity are parameterized based on the bubble diameter, which are used for modeling the local cell-averaged rate of gas dissolution. The dissolution rate is then fed back to the Eulerian transport equation of the bubble mass concentration to account for the reduction of bubble mass due to gas dissolution into surrounding seawater. To test the performance of the new Eulerian-Eulerian gas bubble dissolution modeling approach, the LES model is first applied to simulate a test case with methane bubbles, and the results are compared to the integral model calculation reported from Zheng and Yapa (2002). To further explore the effects of the gas bubble dissolution on the plume dynamics, a series of simulations are conducted with identical volumetric release rate of methane but four different initial bubble diameters. The variation of initial bubble diameter can affect both the gas dissolution rate and the bubble rise velocity, resulting in noticeable variation in the bubble-induced buoyancy force that affects the plume dynamics and material transport. Furthermore, for each initial bubble diameter, both a primary case with gas dissolution modeling and a reference case without gas dissolution effect are simulated to reveal the importance of including the gas dissolution effect in modeling the plume dynamics. In this study, systematic data analyses are performed and the plume statistics under different simulation conditions are compared.

The remainder of this paper is organized as follows. Section 2 provides the detailed description on how to model the gas bubble dissolution effect in the Eulerian-Eulerian LES model. Section 3 shows the results of the test case in which the current LES result is compared to the integral model prediction. Then the LES model is applied to study the effect of initial bubble diameter on the gas dissolution and plume characteristics, and the simulation results are presented in section 4. Finally, conclusions are presented in section 5.

2. Modeling Gas Bubble Dissolution In Eulerian-Eulerian LES Framework

2.1. Modeling Gas Mass Transfer Coefficient

As the gas bubbles from a deep-water blowout rise through the ocean column, they can experience considerable change of seawater hydrostatic pressure and temperature, which can affect the gas state in the bubbles and the gas mass transfer rate from the bubbles into the surrounding seawater. For simplification, in the current study, the gas bubbles are assumed to be in thermal equilibrium with the surrounding seawater so that the temperature in a bubble is the same as the local seawater temperature around it. The bubble surface tension effect is also neglected so that the gas pressure inside the bubbles is assumed to be the same as the hydrostatic pressure in the surrounding seawater. The effect of dynamic pressure due to the motion of the bubble is also neglected because of the dominant contribution from the hydrostatic pressure in the deep-water environment. These simplifications allow us to focus on the development and test of the main methodology for modeling the gas dissolution effect in the Eulerian-Eulerian LES framework. These neglected effects can be included into the LES model framework in the future upon the success of the current gas dissolution model development.

In the current modeling framework, the gas dissolution rate is first modeled for single bubbles (details are given in this section and section 2.2), and then applied to the modeling of the plume by also taking into account the bubble number density (details are given in section 2.3). Due to the high ambient seawater pressure in the deep-water environment, the ideal gas law is not an accurate approximation for describing the state of the gas in the bubbles, and the Peng-Robinson equation of state (Peng & Robinson, 1976; Sloan, 1997) should be used instead (Zheng & Yapa, 2002):

$$p_b V_b = Z n_b R T, \quad (1)$$

where p_b is the pressure inside the bubble, V_b is the volume of a single bubble, Z is the compressibility factor of the gas, n_b is the number of moles of gas in a single bubble, R is the ideal gas constant, and T

is the temperature inside the bubble (which is the same as the seawater temperature under the thermal equilibrium assumption). The key difference between Equation 1 and the ideal gas law is the inclusion of the compressibility factor Z . For bubbles with a single type of gas under a given environment pressure, Z can be calculated by solving a cubic equation constructed based on the equation of state (Peng & Robinson, 1976). The details for determining Z is given in Appendix A.

In order to determine n_b , the evolutions of bubble mass concentration C_b (in kg/m^3) and number density N_b (in m^{-3}) are simulated simultaneously in the LES (details are given in section 2.3). Based on the local values of C_b and N_b and by neglecting the effect of the subgrid-scale bubble size variation, the average value of n_b in each LES computational cell can be calculated based on

$$n_b = \frac{C_b}{N_b M_g}, \quad (2)$$

where M_g is the molar mass of the gas. The cell-averaged single bubble volume within a local LES computational cell, V_b , can be calculated based on Equations 1 and 2 as

$$V_b = \frac{Z n_b R T}{p_b}, \quad (3)$$

and the corresponding equivalent bubble diameter (i.e., for a spherical shape with equal volume) is given by

$$d_e = \sqrt[3]{\frac{6V_b}{\pi}} = \sqrt[3]{\frac{6Z n_b R T}{\pi p_b}}. \quad (4)$$

The gas density in the bubble is given by

$$\rho_b \equiv \frac{n_b M_g}{V_b} = \frac{p_b M_g}{Z R T}. \quad (5)$$

Based on the equivalent bubble diameter d_e , the mass transfer coefficient K (in m/s) for gas dissolution from the bubble to the surrounding seawater can be calculated based on the parameterizations developed from empirical data. In this study, we employ a set of parameterizations for dirty bubbles (i.e., with the effect of surfactant included) for different ranges of d_e based on those used in Zheng and Yapa (2002) and Zhao et al. (2016a). In particular, for small bubbles in the range of $d_e < 4 \times 10^{-4}$ m with spherical shape (Frössling, 1938; Motarjemi & Jameson, 1978; Scala, 2011; Zhao et al., 2016a),

$$\frac{K}{D/d_e} = 0.552 \text{Re}_b^{1/2} \text{Sc}^{1/3}, \quad (6)$$

where d_e is in m, $\text{Sc} = \nu/D$ is the Schmidt number, ν is the kinematic viscosity of seawater (in m^2/s), D is the molecular diffusivity of the gas in the seawater (in m^2/s), $\text{Re}_b = w_{r,b} d_e / \nu$ is the particle Reynolds number, and $w_{r,b}$ is the rise velocity (in m/s) of the gas bubbles relative to the surrounding seawater (which also depends on d_e). For bubbles in the range of 4×10^{-4} m $< d_e < 5 \times 10^{-3}$ m with spherical shape (Tsuchiya et al., 1997; Zhao et al., 2016a),

$$\frac{K}{(D w_{r,b} / d_e)^{1/2}} = \frac{2}{\sqrt{\pi}} \left[\left(1 - \frac{2.89}{\sqrt{\text{Re}_b}} \right) f_R \right]^{1/2}, \quad (7)$$

where f_R is the surface-flow retardation factor given by Tsuchiya et al. (1997)

$$\log_{10} f_R = 0.5 \left\{ \tanh \left[3.9 \log_{10} \left(\frac{d_e}{d_0} \right) \right] - 1 \right\}, \quad (8)$$

with $d_0 = 8.7 \times 10^{-4}$ m. For bubbles in the range of 5×10^{-3} m $< d_e < 1.3 \times 10^{-2}$ m with elliptical shape (Clift et al., 1978, on page 196 underneath Equation 7.50),

$$\frac{K}{D^{1/2}} = A_0, \quad (9)$$

where $A_0 = 6.5 \text{s}^{-1/2}$. For large bubbles in the range of $d_e > 1.3 \times 10^{-2}$ m with spherical cap shape (Clift et al., 1978, page 214, Equation 8.29),

$$\frac{K}{D^{1/2}} = \frac{B_0}{d_e^{1/4}}, \quad (10)$$

where $B_0 = 2.19 \text{m}^{1/4} \text{s}^{-1/2}$ (converted from the original equation in Clift et al., 1978, with d_e in cm).

2.2. Modeling Gas Dissolution Rate for Single Bubble

Using the modeled mass transfer coefficient K , the gas mass dissolution rate of a single bubble, α_b , can be modeled as (Zheng & Yapa, 2002)

$$\alpha_b = A_b K (C_s - C_{dis}), \quad (11)$$

where α_b is in kg/s, K is in m/s, $A_b = \pi d_e^2$ is the bubble equivalent spherical surface area (in m²), C_s is the solubility of the gas in water (in kg/m³), and C_{dis} is the concentration of dissolved gas in the ambient water (in kg/m³). The concentration field C_{dis} is modeled in the LES by solving a transport equation for the dissolved gas part, which is discussed in detail in section 2.3. The solubility is modeled as (Zheng & Yapa, 2002)

$$C_s = \left(\chi \frac{\rho}{M_w} \right) M_g, \quad (12)$$

where χ is the mole fraction of dissolved gas in water at equilibrium condition, ρ is the water density (in kg/m³), M_w is the molar mass of water (in kg/mol), and M_g is the molar mass of gas (in kg/mol).

Considering the high pressure environment near the source of a deep-water blowout, here a modified Henry's law for nonideal gas is applied to model χ (King, 1969; Lekvam & Bishnoi, 1997; Zheng & Yapa, 2002):

$$\chi = \frac{f^g}{H} \exp\left(-\frac{p_b V_m}{RT}\right), \quad (13)$$

where V_m is the gas molar volume (in m³/mol), H is the Henry's law constant (in Pa/mol frac), and f^g is the fugacity of gas in gas phase (in Pa) given by (Peng & Robinson, 1976)

$$f^g = p_b \exp\left[Z - 1 - \ln(Z - B) - \frac{A}{2\sqrt{2}B} \ln\left(\frac{Z + 2.414B}{Z - 0.414B}\right)\right], \quad (14)$$

in which A and B are the model coefficients involved in calculating the compressibility factor Z (see Equations A9 and A10 for more details). Note that Equation 14 is valid for bubbles with a single gas component. If a bubble contains multiple gas components, a variant of Equation 14 needs to be used to calculate the fugacity coefficient for each gas component (see Equation 19 in Peng & Robinson, 1976).

For methane bubble considered in this study, the Henry's law constant H is parameterized as (Carroll & Mather, 1997)

$$H = 1000 \exp\left(\alpha_0 + \frac{\alpha_1}{T} - \frac{\alpha_2}{T^2} + \frac{\alpha_3}{T^3}\right), \quad (15)$$

where the temperature T is in K and the coefficients used in the parameterizations are $\alpha_0 = 5.1345$, $\alpha_1 = 7837$ K, $\alpha_2 = 1.5090 \times 10^6$ K², and $\alpha_3 = 2.060 \times 10^7$ K³. Note that for the sake of model simplification, the effect of salinity is not included in the current calculation, which may result in slight overestimation of H . For future extension of the model, the effect of salinity can be included using the Setchenow equation (Carroll, 1993; Carroll & Mather, 1997; Gros et al., 2016).

2.3. Large-Eddy Simulation Model for Multiphase Hydrocarbon Plume

In the current study, the seawater flow in and around the plume is modeled as a single-phase carrier flow and is simulated using the LES approach. The model uses a Cartesian coordinate system defined as $\mathbf{x} = (x, y, z)$, where x and y are the horizontal coordinates and z is the vertical coordinate. The carrier flow motions are modeled by solving the filtered Navier-Stokes equations (Yang et al., 2016)

$$\nabla \cdot \tilde{\mathbf{u}} = 0, \quad (16)$$

$$\frac{\partial \tilde{\mathbf{u}}}{\partial t} + \tilde{\mathbf{u}} \cdot \nabla \tilde{\mathbf{u}} = -\frac{1}{\rho_0} \nabla \tilde{P} - \nabla \cdot \tilde{\boldsymbol{\tau}}^d + \left(1 - \frac{\tilde{\rho}}{\rho_0}\right) \mathbf{g} \mathbf{e}_z + \left(1 - \frac{\rho_b}{\rho_0}\right) \frac{\tilde{C}_b}{\rho_b} \mathbf{g} \mathbf{e}_z + \left(1 - \frac{\rho_d}{\rho_0}\right) \frac{\tilde{C}_d}{\rho_d} \mathbf{g} \mathbf{e}_z. \quad (17)$$

Here, the tilde denotes the variable resolved by the LES computational grid, $\mathbf{u} = (u, v, w)$ is the velocity vector of the carrier flow, ρ_0 is a reference seawater density, ρ is the local seawater density, P is the modified

pressure, g is the gravitational acceleration, \mathbf{e}_z is the unit vector in the vertical direction, $\boldsymbol{\tau} = (\widetilde{\mathbf{u}\mathbf{u}} - \widetilde{\mathbf{u}}\widetilde{\mathbf{u}})$ is the subgrid-scale stress tensor with $\text{tr}(\boldsymbol{\tau})$ being its trace and $\boldsymbol{\tau}^d = \boldsymbol{\tau} - [\text{tr}(\boldsymbol{\tau})/3]\mathbf{I}$ being its deviatoric part, \mathbf{I} is the identity tensor, ρ_b is the density of gas in bubbles in local LES computational cell, C_b is the mass concentration of gas bubbles, ρ_d is the density of oil droplet, and C_d is the mass concentration of oil droplets. The last three terms in Equation 17 are the buoyancy force due to water density fluctuations, gas bubble concentration, and oil droplet concentration, respectively, which are all modeled based on the Boussinesq approximation (Yang et al., 2016).

Following previous LES studies (e.g., Chen et al., 2018; Kukulka et al., 2010; McWilliams et al., 1997; Polton et al., 2008; Yang et al., 2015), the seawater stratification effect is modeled by considering a virtual potential temperature field θ governed by a filtered convection-diffusion equation

$$\frac{\partial \tilde{\theta}}{\partial t} + \nabla \cdot (\widetilde{\mathbf{u}\theta}) = -\nabla \cdot \boldsymbol{\pi}_\theta, \quad (18)$$

where $\boldsymbol{\pi}_\theta = \widetilde{\mathbf{u}\theta} - \widetilde{\mathbf{u}}\tilde{\theta}$ is the SGS thermal flux. For the sake of model simplification, in the current study, the salinity is assumed to be a constant and the LES-resolved seawater density field $\tilde{\rho}$ is assumed to vary linearly with the potential temperature as (e.g., Kukulka et al., 2010; McWilliams et al., 1997; Polton et al., 2008; Yang et al., 2015)

$$\tilde{\rho} = \rho_0[1 - \alpha_t(\tilde{\theta} - \theta_0)], \quad (19)$$

where α_t is the thermal expansion coefficient and θ_0 is the reference potential temperature corresponding to the reference seawater density ρ_0 .

The evolution of the gas bubble field is described using two continuous Eulerian functions, that is, the bubble number density function $N_b(\mathbf{x}, t)$ and the bubble mass concentration function $C_b(\mathbf{x}, t)$. The evolution of the bubble number density is modeled based on a filtered transport equation

$$\frac{\partial \tilde{N}_b}{\partial t} + \nabla \cdot (\tilde{\mathbf{v}}_b \tilde{N}_b) = -\nabla \cdot \boldsymbol{\pi}_n + q_n, \quad (20)$$

where $\tilde{\mathbf{v}}_b$ is the Lagrangian transport velocity of bubbles, q_n is a volumetric source term (i.e., number of released bubbles per m^3 per second) representing the release of bubbles from a subsea blowout, and $\boldsymbol{\pi}_n = \widetilde{\mathbf{u}N_b} - \widetilde{\mathbf{u}}\tilde{N}_b$ is the SGS flux of bubble number density due to SGS turbulent flow effects. In Equation 20, the effects of bubble breakup and coalescence are neglected for the sake of model simplicity. The bubble transport velocity $\tilde{\mathbf{v}}_b$ is modeled as (Chen et al., 2018; Ferry & Balachandar, 2001; Yang et al., 2016)

$$\tilde{\mathbf{v}}_b = \widetilde{\mathbf{u}} + w_{r,b}\mathbf{e}_z + \frac{w_{r,b}}{g} \frac{D\widetilde{\mathbf{u}}}{Dt}, \quad (21)$$

where $w_{r,b}$ is the rise velocity of bubbles relative to the surrounding carrier flow (see Appendix B for the parameterizations of $w_{r,b}$), and $D\widetilde{\mathbf{u}}/Dt = \partial\widetilde{\mathbf{u}}/\partial t + \widetilde{\mathbf{u}} \cdot \nabla\widetilde{\mathbf{u}}$ is the material derivative (or Lagrangian acceleration) of the carrier flow velocity.

The evolution of the bubble mass concentration field is modeled by solving a filtered transport equation similar to Equation 20 but with the decrease of bubble mass due to the dissolution effect:

$$\frac{\partial \tilde{C}_b}{\partial t} + \nabla \cdot (\tilde{\mathbf{v}}_b \tilde{C}_b) = -\nabla \cdot \boldsymbol{\pi}_b + q_b - \tilde{\alpha}. \quad (22)$$

Here, $\boldsymbol{\pi}_b = \widetilde{\mathbf{u}C_b} - \widetilde{\mathbf{u}}\tilde{C}_b$ is the SGS flux of bubble mass concentration, $q_b = \rho_{b,0}V_{b,0}q_n$ is the volumetric source term for the release of gas bubble mass, $\rho_{b,0}$ is the gas density in the bubbles at the release source, $V_{b,0}$ is the initial volume of a single bubble at the release source, q_n is the same source term for bubble number density as in Equation 20, and $\tilde{\alpha} = \tilde{N}_b\tilde{\alpha}_b$ is the cell-averaged local gas mass dissolution rate (per unit volume) resolved by the LES model. Applying Equation 11 based on the LES-resolved quantities gives

$$\tilde{\alpha} = \tilde{N}_b\tilde{\alpha}_b = \tilde{N}_b\tilde{A}_b\tilde{K}(\tilde{C}_s - \tilde{C}_{dis}). \quad (23)$$

For the dissolved gas in the seawater, the concentration function \tilde{C}_{dis} is modeled using

$$\frac{\partial \tilde{C}_{dis}}{\partial t} + \nabla \cdot (\widetilde{\mathbf{u}C}_{dis}) = -\nabla \cdot \boldsymbol{\pi}_{dis} + \tilde{\alpha}, \quad (24)$$

where $\boldsymbol{\pi}_{dis} = \widetilde{\mathbf{u}}\tilde{C}_{dis} - \tilde{\mathbf{u}}\tilde{C}_{dis}$ is the SGS flux of mass concentration for the dissolved gas. Unlike \tilde{N}_b and \tilde{C}_b , the concentration \tilde{C}_{dis} for the dissolved gas is transported as a passive scalar based on the carrier flow velocity $\tilde{\mathbf{u}}$. Note that the evolution equations for \tilde{C}_b and \tilde{C}_{dis} are coupled through the gas dissolution rate $\tilde{\alpha}$, which acts as a sink term in Equation 22 and as a source term in Equation 24.

In addition, we also simulate the transport of dye and oil droplets to model the effects of the plume on transporting materials. The evolution of the dye mass concentration field \tilde{C}_{dye} is used to represent the transport of passive tracers, which is governed by the filtered transport equation

$$\frac{\partial \tilde{C}_{dye}}{\partial t} + \nabla \cdot (\tilde{\mathbf{u}}\tilde{C}_{dye}) = -\nabla \cdot \boldsymbol{\pi}_{dye} + q_{dye}, \quad (25)$$

where q_{dye} is a source term for the dye release and $\boldsymbol{\pi}_{dye} = (\widetilde{\mathbf{u}}\tilde{C}_{dye} - \tilde{\mathbf{u}}\tilde{C}_{dye})$ is the SGS dye concentration flux. The transport of oil droplets is affected by both the carrier flow and the buoyancy-induced rise velocity of the oil droplets. The oil droplet mass concentration field \tilde{C}_d is modeled by solving the filtered transport equation

$$\frac{\partial \tilde{C}_d}{\partial t} + \nabla \cdot (\tilde{\mathbf{v}}_d\tilde{C}_d) = -\nabla \cdot \boldsymbol{\pi}_d + q_d, \quad (26)$$

where q_d is a source term for the oil droplet release, $\boldsymbol{\pi}_d = (\widetilde{\mathbf{u}}\tilde{C}_d - \tilde{\mathbf{u}}\tilde{C}_d)$ is the SGS flux of oil mass concentration, and $\tilde{\mathbf{v}}_d$ is the transport velocity of oil droplets (with nonnegligible buoyancy effect) (e.g., Chen et al., 2016; Chor et al., 2018; Yang et al., 2015):

$$\tilde{\mathbf{v}}_d = \tilde{\mathbf{u}} + w_{r,d}\mathbf{e}_z + \frac{w_{r,d}}{g} \frac{D\tilde{\mathbf{u}}}{Dt}. \quad (27)$$

The oil droplet rise velocity due to buoyancy is modeled as (Clift & Gauvin, 1971; Veron, 2015; Yang et al., 2016)

$$w_{r,d} = \begin{cases} w_{r,d}^S & \text{Re}_d < 0.2, \\ w_{r,d}^S (1 + 0.15\text{Re}_d^{0.687})^{-1} & 0.2 < \text{Re}_d < 750, \end{cases} \quad (28)$$

where $w_{r,d}^S$ is the oil droplet rise velocity given by Stokes' law as

$$w_{r,d}^S = \frac{(1 - \rho_d/\rho_0)gd_d^2}{18\nu}, \quad (29)$$

where ρ_d is the oil density, d_d is the equivalent diameter of the oil droplet, ν is the kinematic viscosity of water, and $\text{Re}_d = w_{r,d}d_d/\nu$ is the oil droplet Reynolds number.

Following Yang et al. (2014–2016), the filtered LES governing equations 17, 18, 20, 22, and 24–26 are closed by parameterizing the SGS terms with proper turbulence closures. In particular, the SGS stress tensor $\boldsymbol{\tau}^d$ is parameterized using the Lilly–Smagorinsky eddy-viscosity type model (Lilly, 1967; Smagorinsky, 1963), $\boldsymbol{\tau}^d = -2\nu_\tau\tilde{\mathbf{S}}$, where $\tilde{\mathbf{S}} = [\nabla\tilde{\mathbf{u}} + (\nabla\tilde{\mathbf{u}})^T]/2$ is the resolved strain rate tensor, $\nu_\tau = (c_s\Delta)^2|\tilde{\mathbf{S}}|$ is the modeled SGS eddy viscosity, c_s is the Smagorinsky model coefficient, and Δ is the LES grid (filter) scale. In the current model, the value of c_s is determined dynamically during the simulation using the Lagrangian-averaged scale-dependent dynamic SGS model (Bou-Zeid et al., 2005). The SGS fluxes of the scalar quantities are then parameterized as $\boldsymbol{\pi}_\theta = -(\nu_\tau/\text{Pr}_\tau)\nabla\tilde{\theta}$, $\boldsymbol{\pi}_n = -(\nu_\tau/\text{Sc}_\tau)\nabla\tilde{N}_b$, $\boldsymbol{\pi}_b = -(\nu_\tau/\text{Sc}_\tau)\nabla\tilde{C}_b$, $\boldsymbol{\pi}_{dis} = -(\nu_\tau/\text{Sc}_\tau)\nabla\tilde{C}_{dis}$, and $\boldsymbol{\pi}_{dye} = -(\nu_\tau/\text{Sc}_\tau)\nabla\tilde{C}_{dye}$, with a constant SGS Prandtl number $\text{Pr}_\tau = 0.4$ and SGS Schmidt number $\text{Sc}_\tau = 0.4$ (Antonopoulos-Domis, 1981; Chamecki et al., 2009; Kumar et al., 2006; Mason & Journal of the Atmospheric Sciences, 1989; Moeng, 1984; Sullivan et al., 1994; Yang et al., 2016). The solution process and numerical schemes for solving the LES model equations are summarized in Appendix C.

3. LES Gas Dissolution Model Test

The basic coupled turbulent flow and scalar transport solver used in the current LES model has been tested against experimental data (Chamecki et al., 2009) and successfully applied to simulate oil and gas plume dispersion in the oceanic environment in several prior studies (e.g., Chen et al., 2016; Chor et al., 2018; Yang et al., 2015). The LES solver's performance has been further tested against laboratory experiments for bubble-driven plume (Seol et al., 2009) and oil jet in cross flow (Murphy et al., 2016) in several recent studies

Table 1
List of Large-Eddy Simulation Cases

Case	Gas dissolution	Stratification	$d_{e,0}$	Grid number	Time step
LS-12D-L	Modeled	Linear	12 mm	$192 \times 192 \times 256$	0.2 s
LS-12D-M	Modeled	Linear	12 mm	$256 \times 256 \times 320$	0.1 s
LS-12D0-M	Modeled ^a	Linear	12 mm	$256 \times 256 \times 320$	0.1 s
LS-12N-M	Not modeled	Linear	12 mm	$256 \times 256 \times 320$	0.1 s
LS-12D-H	Modeled	Linear	12 mm	$320 \times 320 \times 384$	0.1 s
QS-3D	Modeled	Quadratic	3 mm	$256 \times 256 \times 320$	0.1 s
QS-6D	Modeled	Quadratic	6 mm	$256 \times 256 \times 320$	0.1 s
QS-12D	Modeled	Quadratic	12 mm	$256 \times 256 \times 320$	0.1 s
QS-18D	Modeled	Quadratic	18 mm	$256 \times 256 \times 320$	0.1 s
QS-3N	Not modeled	Quadratic	3 mm	$256 \times 256 \times 320$	0.1 s
QS-6N	Not modeled	Quadratic	6 mm	$256 \times 256 \times 320$	0.1 s
QS-12N	Not modeled	Quadratic	12 mm	$256 \times 256 \times 320$	0.1 s
QS-18N	Not modeled	Quadratic	18 mm	$256 \times 256 \times 320$	0.1 s

Note. In the table, $d_{e,0}$ is the initial equivalent bubble diameter at the plume source.

^aIn case LS-12D0-M, the methane is treated as ideal gas.

(e.g., Aiyer et al., 2019; Yang et al., 2016). Here, we focus on testing the performance of the new LES model for capturing the gas dissolution effect.

In the test case, the physical parameters of the environmental and plume conditions were set to match with those used in the integral plume model computation in Zheng and Yapa (2002). In particular, the seawater temperature was assumed to vary linearly with the depth

$$T(z) = T_b + \gamma z, \quad 0 \leq z \leq L_z, \quad (30)$$

where γ is the vertical temperature gradient, T_b is the seawater temperature at the bottom of the simulation domain (i.e. at $z = 0$ m), and L_z is the domain height. Following Zheng and Yapa (2002), these parameters were set to be $\gamma = 0.02 \text{ K m}^{-1}$, $T_b = 284.15 \text{ K}$, and $L_z = 700 \text{ m}$. Following Zheng and Yapa (2002), a constant salinity of 35‰ was considered and the corresponding background density stratification was set up accordingly. In the test case, methane bubbles with a uniform initial equivalent diameter of $d_{e,0} = 12 \text{ mm}$ were released from a localized source at $z = 0 \text{ m}$ with a volume release rate of $Q_v^0 = 3.2752 \text{ normal m}^3/\text{s}$ (i.e., defined under normal condition at the sea level) (Zheng & Yapa, 2002). The corresponding mass release rate of methane is $Q_c = 2.32 \text{ kg/s}$. Oil droplets with density $\rho_d = 893 \text{ kg/m}^3$ and diameter $d_d = 0.5 \text{ mm}$ were also released from the same source location with a mass release rate of 16.4 kg/s. In addition, the dye (i.e., passive tracer) was released from the source with a mass release rate of 1 g/s.

In the test case, a domain of $(L_x, L_y, L_z) = (700, 700, 700) \text{ m}$ was used for the LES. Three test runs with different grid numbers for the spatial discretization were considered, including a coarse-grid case with $N_x \times N_y \times N_z = 192 \times 192 \times 256$ points, a medium-grid case with $256 \times 256 \times 320$ points, and a fine-grid case with $320 \times 320 \times 384$ points. These three cases are named as LS-12D-L, LS-12D-M, and LS-12D-H, respectively. The simulation time steps used for these LES runs with different grid resolutions were $\Delta t = 0.2 \text{ s}$ for the coarse-grid case, and 0.1 s for the medium- and fine-grid cases. The simulations cases for the current test as well as for the results reported in section 4 are listed in Table 1. Similar to the LES study reported in Yang et al. (2016), we used the no-slip condition at the bottom boundary, the free-slip condition at the top boundary, and the periodic boundary conditions in the horizontal directions associated with the pseudo-spectral method. Note that Yang et al. (2016) obtained good agreement with the laboratory experimental data of Seol et al. (2009) by performing LES using a domain with an aspect ratio of 0.67 : 0.67 : 1 (for $L_x : L_y : L_z$), which was found to be sufficient to avoid artificial effect from the periodic horizontal boundary conditions. The current domain aspect ratio of 1 : 1 : 1 is expected to provide sufficient horizontal space for the expansion of the horizontal intrusion layers from the plume.

The general dynamics of multiphase buoyancy plume in stratified flow environment has been studied experimentally and numerically in prior studies (Crouse et al., 2007; Lemckert & Imberger, 1993; Richards et al.,

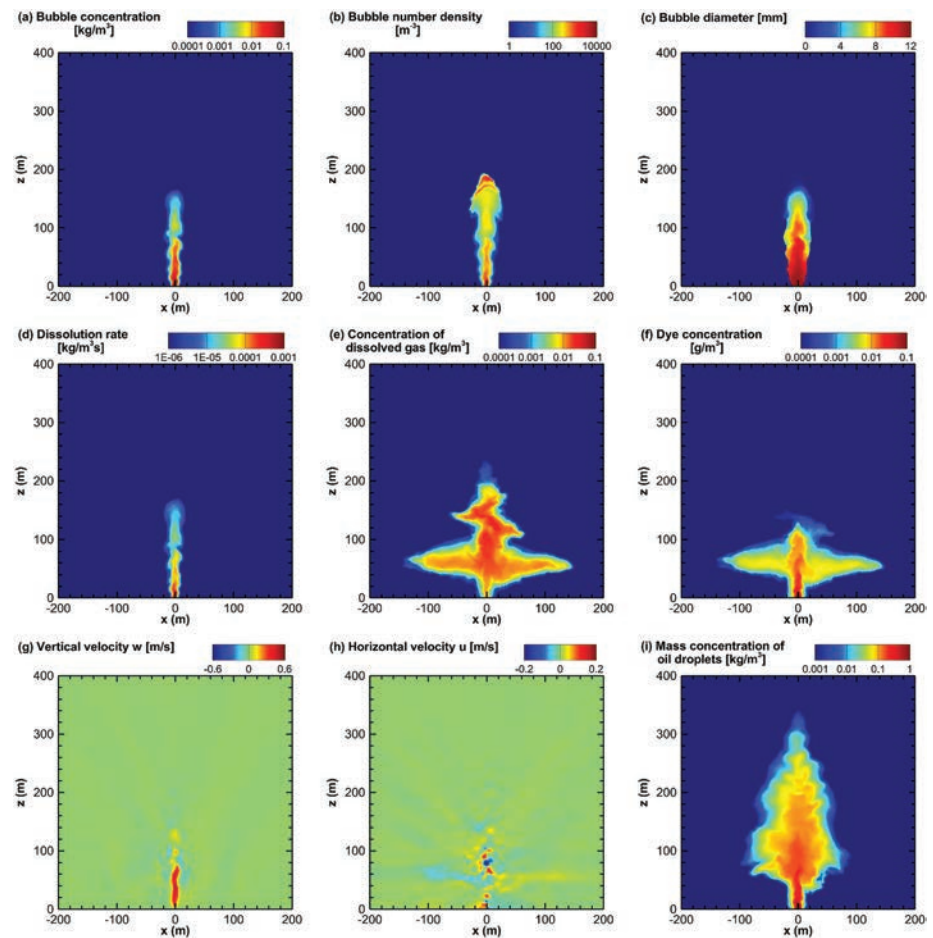


Figure 1. Instantaneous plume flow and scalar fields for case LS-12D-M obtained from the LES. Here, the contours on the (x, z) -plane across the center of the plume are shown: (a) bubble mass concentration (in kg/m^3); (b) bubble number density (in m^{-3}); (c) bubble diameter (in mm); (d) bubble mass dissolution rate (in $\text{kg/m}^3\text{s}$); (e) mass concentration of dissolved gas in the water (in kg/m^3); (f) dye concentration (in g/m^3); (g) vertical velocity of plume flow (in m/s); (h) horizontal velocity of plume flow (in m/s); (i) oil droplets mass concentration (in kg/m^3).

2014; Socolofsky & Adams, 2003; Socolofsky et al., 2008; Seol et al., 2009; Yang et al., 2016). Here, the physical processes are briefly summarized. The multiphase plume consisting of methane bubbles, oil droplets, and dye tracer is released from a localized source at the initial time $t = 0$ s. Due to the density difference between the methane bubbles and the ambient seawater, the buoyancy induced by the bubbles provides the main driving force for the multiphase plume to rise upwards. The turbulence eddies entrain the ambient seawater into the plume as it rises and lifts the entrained seawater to higher elevations where the ambient seawater has smaller density due to the stable stratification. The density difference between the entrained and ambient seawater results in a downward force to act against the buoyancy induced by the bubbles. In the meantime, the methane in the bubbles gets dissolved continuously into the surrounding seawater, causing the plume to lose the buoyancy when rising. Once the plume reaches a height where the downward force due to entrained seawater can overcome the buoyancy from the remaining gas bubbles, the entrained seawater in the plume starts to slow down and eventually reaches the maximum rising elevation, from where the heavier entrained seawater peels from the inner rising plume to form an annular plume that falls down along the outside of the inner rising plume (Asaeda & Imberger, 1993; Socolofsky & Adams, 2003; Socolofsky et al., 2016).

Figure 1 shows a representative snapshot of the plume structure at $t = 8,000$ s, in which the contours of several key physical quantities obtained from the LES are shown on the (x, z) -plane across the plume center line. The LES model obtains the instantaneous bubble mass concentration C_b (Figure 1a) and number density N_b (Figure 1b) by solving their transport equations, based on which the local cell-averaged bubble

diameter (Figure 1c) and bubble gas dissolution rate (Figure 1d) are modeled. The methane gas in the bubbles gets dissolved into the surrounding seawater at the modeled instantaneous gas mass dissolution rate, causing the bubble diameter to reduce with height from the source (Figure 1c). Consequently, the bubble mass concentration (Figure 1a) decreases as the plume rises and becomes negligible above $z = 180$ m. In the height range of $180 \text{ m} \lesssim z \lesssim 200$ m, the bubble number density (Figure 1b) appears to be high due to the accumulation of tiny bubbles, which have negligible rise velocities and buoyancy effects. These tiny bubbles are found to be fully dissolved below $z = 200$ m.

The plume dynamics can be seen from the contours of the vertical velocity w (Figure 1g) and horizontal velocity u (Figure 1h). The plume is released with zero initial velocity right at the source but quickly reaches a noticeable vertical velocity due to the bubble-induced buoyancy. The horizontal gradient of the vertical velocity induces the shear instability and generates turbulent motions as the plume rises, causing the fluctuation of the horizontal velocity that entrains ambient seawater into the plume to rise together with the methane bubbles and oil droplets. Due to the stable stratification of the ambient environment, the seawater entrained at lower elevation has higher density than the surrounding environment when lifted to higher elevations by the plume, resulting in a downward force to the plume flow (i.e., the first Boussinesq term on the right-hand side of Equation 17). This downward force caused by density stratification increases as the entrained seawater rises while the buoyancy of bubbles decreases with height due to the continuous gas dissolution, which causes the plume to decelerate and eventually start falling at around $z = 140$ m. This maximum height of the plume rise is named the peel height (Socolofsky & Adams, 2005). The higher density seawater entrained into the plume at lower elevation detrains from the plume at the peel height to form an annular downward plume outside the inner rising plume, as indicated by the negative vertical velocity in Figure 1g. The peeling process is unsteady due to the highly dynamic interactions and counter motions between the inner and outer plumes, which has been studied in detail in previous studies (Seol et al., 2009; Yang et al., 2016).

During the strong peeling process, the dissolved methane (Figure 1e) and dye (Figure 1f) are carried by the detrained seawater to fall together along the downward outer plume and then transported horizontally to form an intrusion layer at around $z = 60$ m where the detrained seawater reaches the new equilibrium height in density. Note that the dye concentration is negligible above $z = 140$ m, indicating that most of the seawater entrained and carried by the plume from lower elevation near the source gets detrained from the rising plume at the peel height at $z = 140$ m. This is consistent with the large peeling fraction in deep-sea blowout condition reported in Socolofsky et al. (2011). Note that when the remaining undissolved gas bubbles continue to rise up to $z = 200$ m (Figure 1b) before getting fully dissolved, they continue to contribute to the concentration of the dissolved gas (Figure 1e), allowing us to visualize the secondary peel and intrusion events above the primary peel height ($z = 140$ m) that is not visible from the contours of the dye concentration (Figure 1f).

The oil droplets with 0.5 mm diameter behave differently from other passive scalars (e.g., dye and dissolved gas) in the plume. Initially the oil droplets rise upwards along the narrow inner plume together with the bubbles and entrained seawater. At the peel height, the oil column expands horizontally due to the horizontal velocity associated with the peeling process. Additional entrainment of the oil droplet from the inner plume also occurs below the primary peel height (at $z = 140$ m) due to the turbulence in the shear layer between the inner and outer plumes. The combined effect of the peeling and turbulent entrainment processes results in a noticeable expansion of the oil column starting from $z = 40$ m. Different from passive scalars, the oil droplets have small but nonnegligible rise velocity relative to the surrounding seawater flow. As a result, the oil droplets can escape from the falling outer plume and continue to rise slowly by its own buoyancy even after all the gas bubbles are fully dissolved. Similar behavior of the oil droplet plume was observed in the laboratory study of Chan et al. (2015) in their Type-1a* plumes.

Figure 2 shows the mean bubble diameter inside the inner plume as a function of the vertical elevation. Here, the mean bubble diameter at the elevation z is estimated as

$$[d_e](z) = \left(\frac{6 \int_0^{b_i} \langle \tilde{C}_b \rangle 2\pi r \, dr}{\pi \rho_b \int_0^{b_i} \langle \tilde{N}_b \rangle 2\pi r \, dr} \right)^{1/3}, \quad (31)$$

where b_i is the radius of the averaged inner plume and $\langle \tilde{C}_b \rangle$ and $\langle \tilde{N}_b \rangle$ are the time- and angular-averaged bubble mass concentration and number density, respectively. The predictions from the integral model of

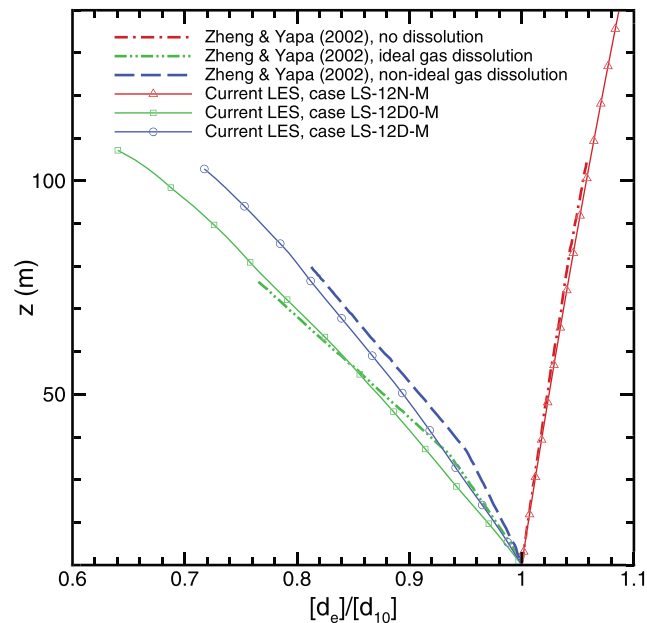


Figure 2. Variation of bubble diameter with height. The LES results for three different simulation conditions are plotted: case LS-12N-M (without gas dissolution), case LS-12D0-M (with gas dissolution based on ideal gas law), and case LS-12D-M (with gas dissolution based on nonideal gas law). The corresponding integral model predictions from Zheng and Yapa (2002) are also plotted for comparison. The equivalent bubble diameter d_e is normalized by the reference diameter d_{10} at $z = 10$ m above the plume source.

Zheng and Yapa (2002) are also included in Figure 2. Note that in Zheng and Yapa (2002), three different integral model computations were performed, including the primary case with gas dissolution based on the modified Henry's law for nonideal gas under the deep-water environment, as well as a case with gas dissolution based on Henry's law for ideal gas and a case without gas dissolution. For comparison, the LES runs were performed accordingly by matching the physical parameters as well as the gas dissolution setting. Note that in the integral model of Zheng and Yapa (2002), the initial effect of heat transfer between the hot gas bubbles and the ambient seawater was included, resulting in the thermal shrinkage of the bubbles within the first few meters above the plume source. This effect is not included in the current LES model for the sake of model simplicity. Here, the comparisons between the current LES model results and the integral plume model prediction by Zheng and Yapa (2002) are made for the region above the initial thermal shrinkage region, and the bubble diameters shown in Figure 2 are normalized by the corresponding mean bubble diameter at 10 m above the source in each case. Above this initial shrinkage region, the case without gas dissolution (i.e., case LS-12N-M) exhibits a monotonic increase of bubble diameter with height due to the reduction of the ambient hydrostatic pressure, while the cases with gas dissolution (i.e., cases LS-12D-M and LS-12D0-M) show a monotonic decrease of bubble diameter with height. The use of the regular Henry's law for ideal gas in case LS-12D0-M results in an overestimation of the gas dissolution rate, causing the predicted bubble diameter to reduce more rapidly than that predicted in case LS-12D-M using the modified Henry's law for nonideal gas. The current LES model shows good agreement with the integral model of Zheng and Yapa (2002) for modeling the gas bubble size variation due to gas dissolution and change of hydrostatic pressure. Considering the complexities associated with modeling the plume dynamics and gas mass transfer process, the overall agreement between the two models are considered to be satisfactory.

To test the grid resolution convergence of the LES model, here the simulation results from the cases LS-12D-L ($192 \times 192 \times 256$ grid points), LS-12D-M ($256 \times 256 \times 320$ grid points), and LS-12D-H ($320 \times 320 \times 384$ grid points) are compared. Figure 3 shows the gas bubble concentration, vertical velocity of plume flow, and oil droplet concentration of the time- and angular-averaged plume obtained from these three LES cases. Overall, the LES model results exhibit consistent mean plume structures for the three grid resolutions tested here. Figure 4 compares the vertical variations of the bubble diameter along the center line of the time- and angular-averaged plume from the three LES cases, and Figure 5 shows the vertical distributions of total masses of gas bubbles and oil droplets per unit depth. The LES model obtains consistent trends for the

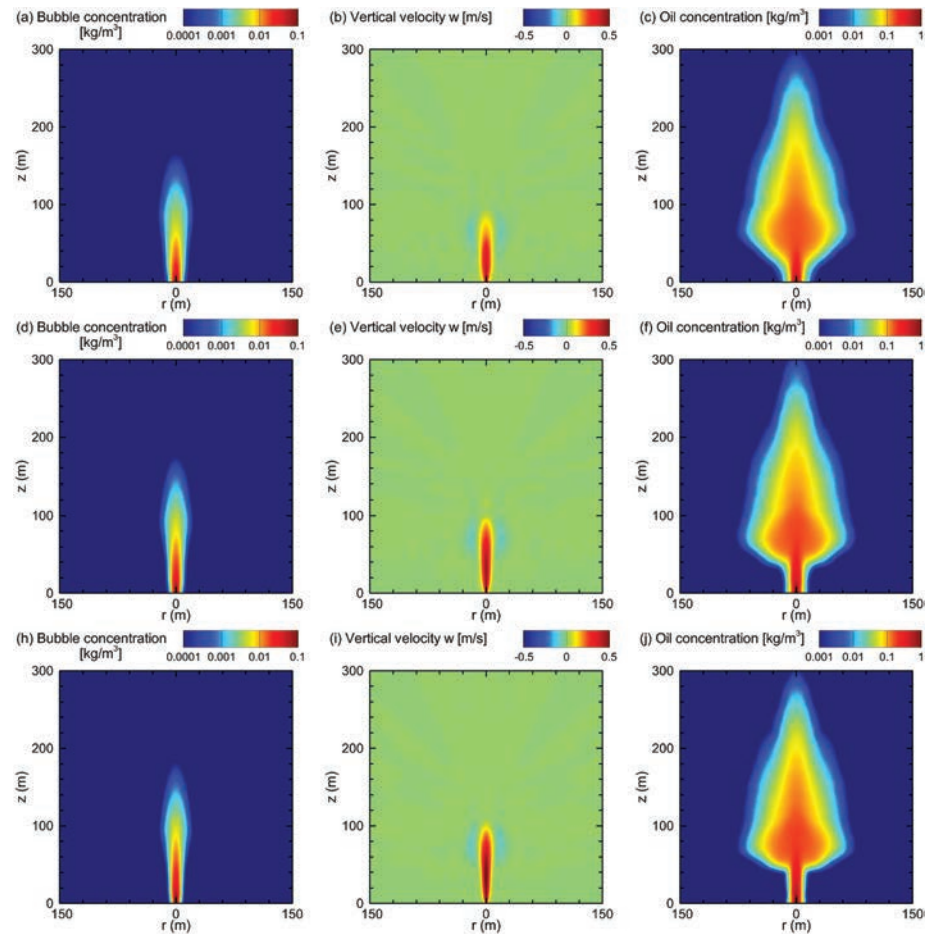


Figure 3. Comparison of time- and angular-averaged plume flow and scalar fields from LES runs with different grid resolutions: (a–c) case LS-12D-L ($192 \times 192 \times 256$ grid points); (d–f) case LS-12D-M ($256 \times 256 \times 320$ grid points); (h–j) case LS-12D-H ($320 \times 320 \times 384$ grid points). For each LES case, the left panel shows the bubble mass concentration (in kg/m^3), the middle panel shows the vertical velocity of the plume flow (in m/s), and the right panel shows the oil droplets mass concentration (in kg/m^3).

center-line bubble diameter as well as the vertical distributions of bubble/droplet masses with the three different grid resolutions. Cases LS-12D-M and LS-12D-H are found to agree fairly well considering the overall complexity of the plume physics and the LES model, which suggests that the medium grid resolution (i.e., with $256 \times 256 \times 320$ grid points) is sufficient for accurately modeling the gas bubble dissolution and capturing its effect on the plume dynamics. Therefore, for other simulation cases reported in this paper (see Table 1), the medium grid resolution instead of the high grid resolution is used for the sake of limiting the overall computational cost associated with conducting the simulations and data analyses.

4. Effects of Gas Dissolution and Initial Bubble Size on Plume Dynamics

The test case with linear seawater stratification discussed in section 3 shows that the new LES gas dissolution model developed in the current study can capture the essential dynamics of the multiphase hydrocarbon plume in the deep-water environment. In this section, the LES model is applied to study the effects of gas dissolution and initial bubble size on the near-field plume dynamics. Similar to the test case in section 3, a domain of $(L_x, L_y, L_z) = (700, 700, 700)$ m was used for all the LES cases reported in this section. $N_x \times N_y \times N_z = 256 \times 256 \times 320$ grid points were used for the spatial discretization and the time step was set to be 0.1 s.

Note that in order to match the parameters used in the integral model, the test case reported in section 3 uses the same idealized linear seawater stratification considered by Zheng and Yapa (2002). For the LES cases reported in this section, more realistic seawater CDT profiles based on the field data from the Gulf of Mexico R/V Brooks McCall at Station B54 ($28^\circ 43.945' \text{N}$, $88^\circ 22.607' \text{W}$; 30 May 2010) is used. In particular,

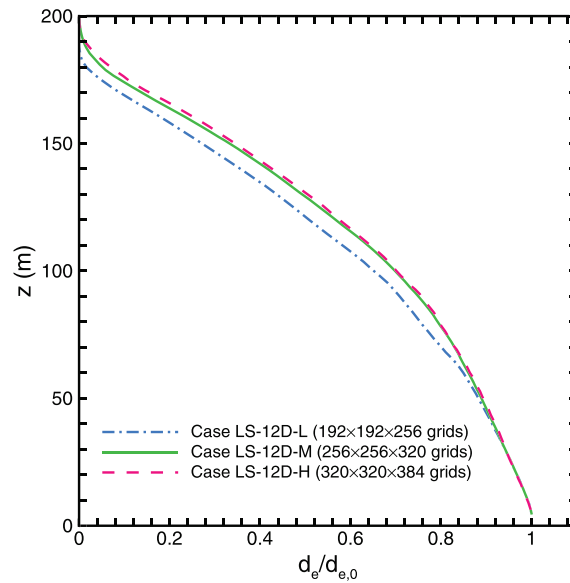


Figure 4. Vertical variation of bubble diameter along the center line of the time- and angular-averaged plume obtained from the LES runs with different grid resolutions: case LS-12D-L ($192 \times 192 \times 256$ grid points), case LS-12D-M ($256 \times 256 \times 320$ grid points), and case LS-12D-H ($320 \times 320 \times 384$ grid points).

the density stratification has a quadratic profile of (Socolofsky et al., 2011)

$$\rho_w(z) = 1027.77 - 4.60434 \times 10^{-7} \times (z + 800)^2, \quad (32)$$

where the vertical coordinate z has the origin at the 700-m depth just as in the test case shown in section 3. In the simulation, Equation 32 was used to initialize the seawater density. During the simulation, the seawater density field varies dynamically in time and space according to Equations 19 and 18 for modeling the effect of stratification on the plume dynamics. The temperature profile used in the calculation of the gas dissolution rate (see sections 2.1 and 2.2) were prescribed based on

$$T(z) = 396.2216 \times (700 - z)^{-0.6205} + 273.15. \quad (33)$$

which can be obtained by fitting the temperature data from the R/V Brooks McCall at Station B54 between the 100- and 1,546-m depth. Note that using the prescribed temperature profile in Equation 33 instead of the instantaneous local temperature from the LES allows us to perform the calculation of gas compressibility factor Z once at the beginning of the simulation instead of performing the calculation at each time step. For

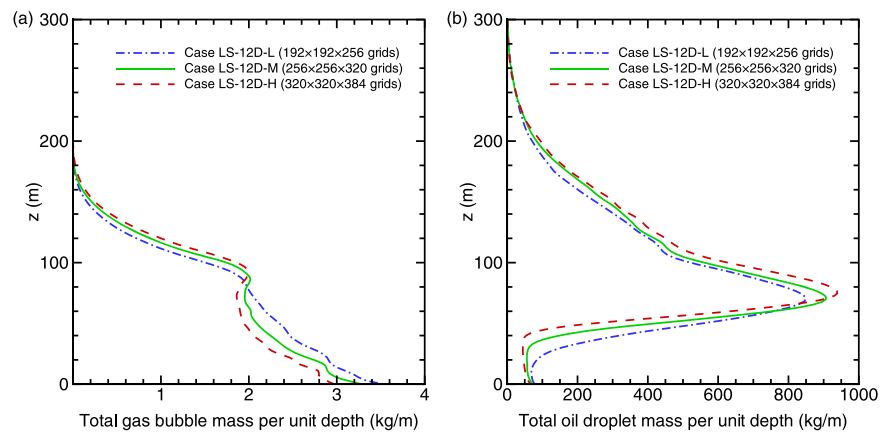


Figure 5. Vertical distributions of mass of (a) gas bubbles and (b) oil droplets in the time- and angular-averaged plume obtained from the LES runs with different grid resolutions: case LS-12D-L ($192 \times 192 \times 256$ grid points), case LS-12D-M ($256 \times 256 \times 320$ grid points), and case LS-12D-H ($320 \times 320 \times 384$ grid points).

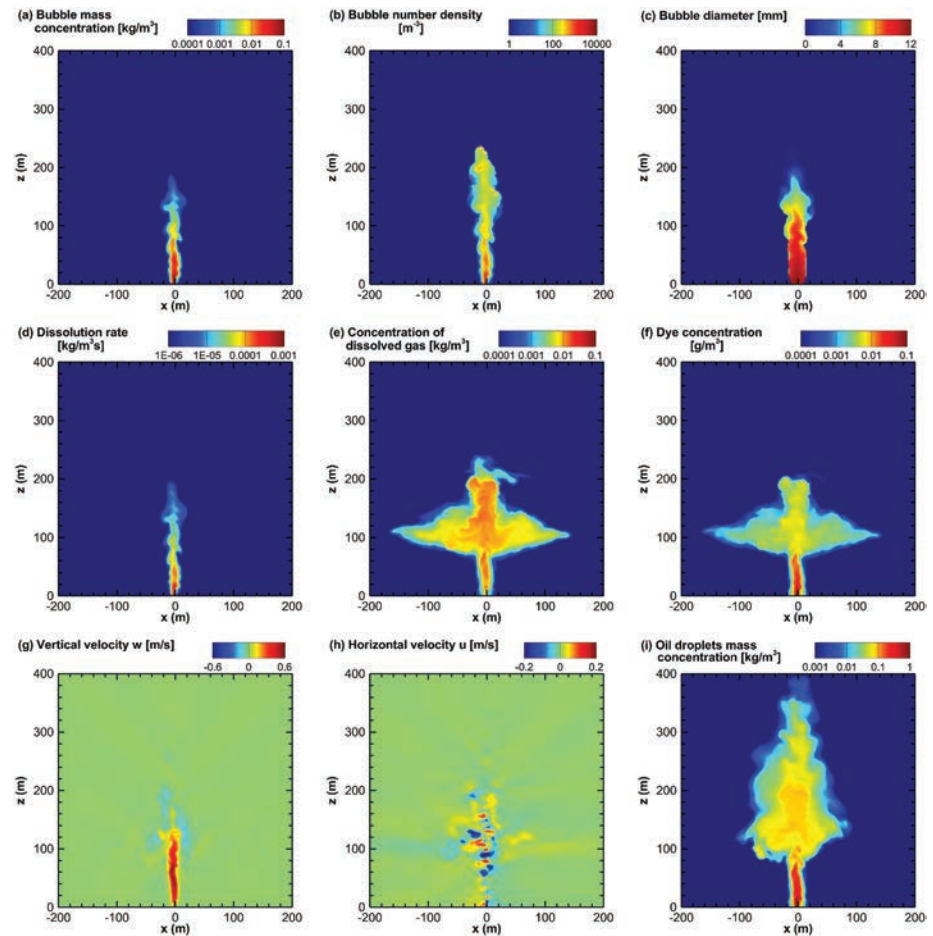


Figure 6. Instantaneous plume flow and scalar fields for case QS-12D obtained from the LES. Here, the contours on the (x, z) -plane across the center of the plume at $t = 8,000$ s are shown: (a) bubble mass concentration (in kg/m^3); (b) bubble number density (in m^{-3}); (c) bubble diameter (in mm); (d) bubble mass dissolution rate (in $\text{kg/m}^3\text{s}$); (e) mass concentration of dissolved gas in the water (in kg/m^3); (f) dye concentration (in g/m^3); (g) vertical velocity of plume flow (in m/s); (h) horizontal velocity of plume flow (in m/s); (i) oil droplets mass concentration (in kg/m^3).

the results reported in this section, this simplification only causes error in the estimated gas dissolution rate for less than $\sim 1\%$ for the reported cases but can significantly reduce the computational cost.

To further explore the effects of gas bubble dissolution on the near-field plume dynamics, four different initial bubble diameters were considered, including $d_{e,0} = 3$ mm, 6 mm, 12 mm, and 18 mm, which are referred to as the cases QS-3D, QS-6D, QS-12D, and QS-18D, respectively. For each initial bubble diameter, an additional reference case without considering gas dissolution was simulated for comparison purpose. These four reference cases are referred to as the cases QS-3N, QS-6N, QS-12N, and QS-18N, respectively. Table 1 summarizes the eight simulation cases considered in this section. In these eight cases, other simulation parameters (such as the simulation domain size, the source release rates of gas bubbles, oil droplets, and dye) were set to be identical to the test cases reported in section 3.

Figure 6 shows the instantaneous flow and scalar fields of case QS-12D on the (x, z) -plane across the center line of the plume at $t = 8,000$ s. Note that case QS-12D has a weaker density stratification near the source (due to the quadratic density profile) than that in case LS-12D-M, while other simulation parameters are identical between the two cases. Consequently, the basic structures of the instantaneous plume appear to be similar between the two cases, but the peel and trap heights as well as the maximum elevation of the gas bubbles in case QS-12D are higher than the corresponding ones in the test case LS-12D-M.

Figure 7 compares some of the instantaneous plume features (i.e., the mass concentrations of the bubbles, dye and oil droplets) between case QS-12N (without gas dissolution) and case QS-12D (with gas dissolution).

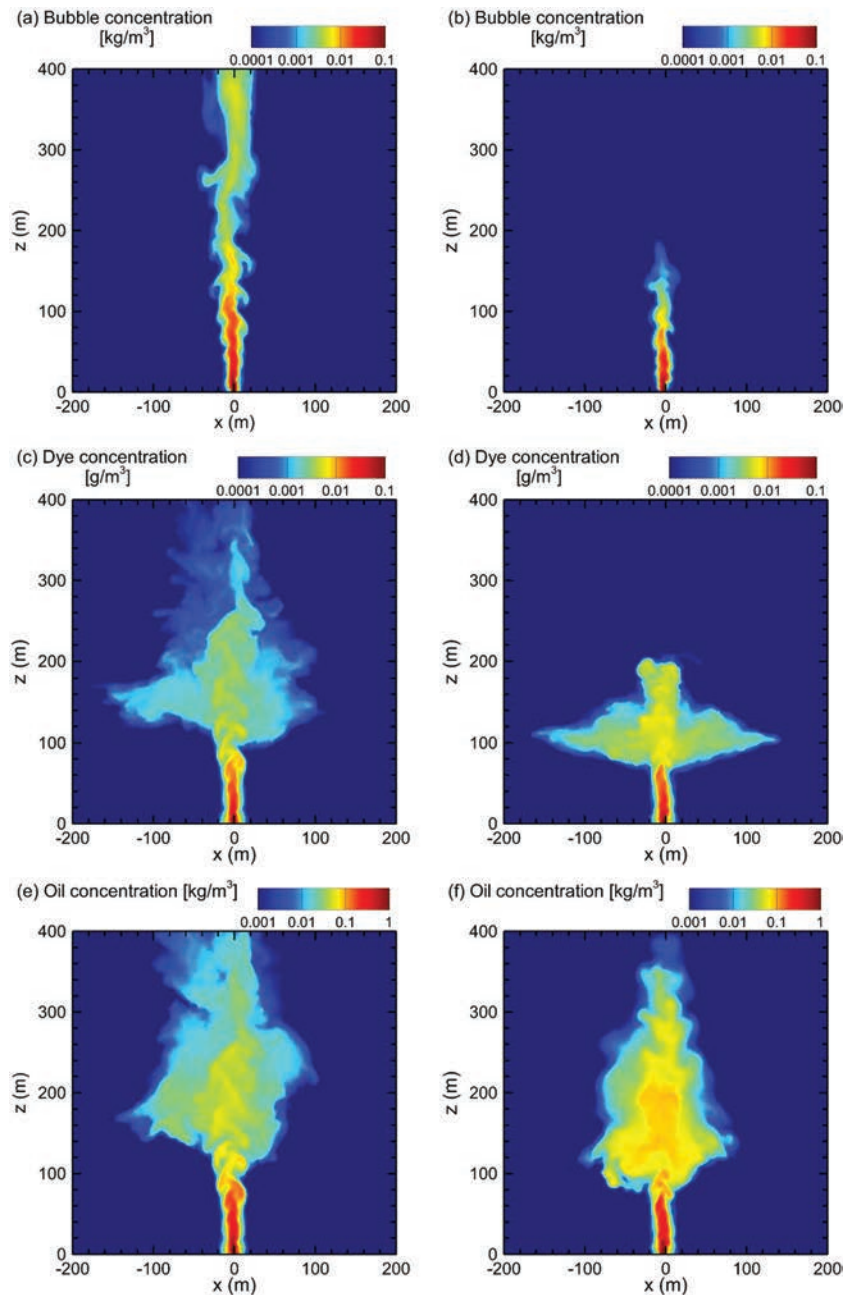


Figure 7. Comparison of the instantaneous plume features between case QS-12N (without gas dissolution) (a,c,e) and case QS-12D (with gas dissolution) (b,d,f). Panels (a) and (b) show the bubble mass concentration \tilde{C}_b (in kg/m^3); panels (c) and (d) show the dye concentration \tilde{C}_{dye} (in g/m^3); panels (e) and (f) show the oil droplet mass concentration \tilde{C}_d (in kg/m^3). Here, the contours on the (x, z) -plane across the center of the plume are shown.

Without considering the gas dissolution effect, the simulation results from case QS-12N show that the gas bubbles rise continuously toward the ocean surface, with the local gas concentration diluted due to the turbulent entrainment as well as the horizontal motions in the peeling region at around $z = 300$ m (Figure 7a). The persistence of the bubble buoyancy without the gas dissolution effect also causes the plume flow motion to be strong, resulting in strong turbulent mixing between the rising inner plume and the falling outer plume as well as the ambient environment as shown by the diluted dye and oil concentrations in $100 \text{ m} < z < 400 \text{ m}$ (Figures 7c and 7e). In contrast, the gas dissolution effect considered in case QS-12D causes the gas bubbles to be fully dissolved below $z = 200$ m (Figure 7b), resulting in a distinct maximum elevation of the dye at around $z = 200$ m when the entrained seawater peels from the plume and falls down along the outer plume

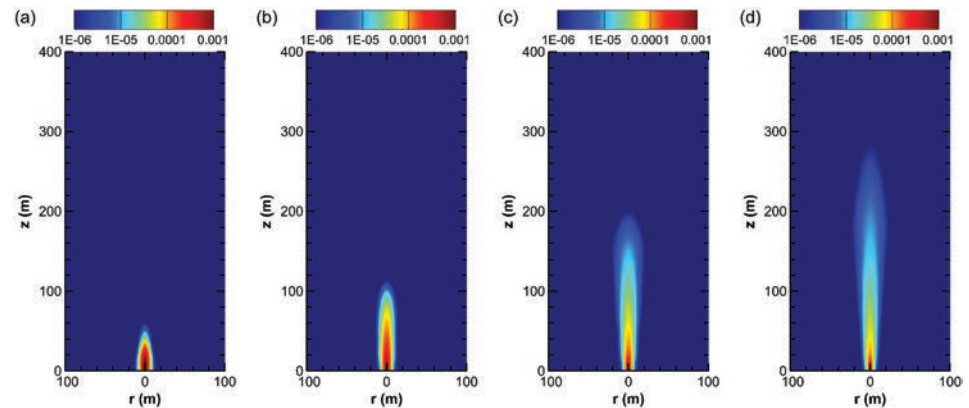


Figure 8. Angular- and time-averaged bubble gas mass dissolution rate α (in $\text{kg}/\text{m}^3\text{s}$): (a) case QS-3D; (b) case QS-6D; (c) case QS-12D; (d) case QS-18D.

after the plume loses all the driving force from the bubble buoyancy (Figure 7d). Above the peel height (around $z = 200$ m), in case QS-12D, the vertical velocity of the plume fluid has vanished (Figure 6g) and the oil droplets continue to rise due to their own buoyancy (Figure 7f).

To make more quantitative comparison among different simulation cases with and without gas dissolution, time- and angular-average is performed to obtain the mean plume structure within $0 \leq z \leq 400$ m. In particular, 400 three-dimensional instantaneous snapshots of the plume (sampled between $t = 4,000$ and $20,000$ s with a constant time interval of 40 s) are used as the samples for time average for each simulation case, and each time-averaged field is further averaged in the angular direction considering the axisymmetry of the mean plume structure (Yang et al., 2016). Note that for computing the mean oil concentration field, only the 100 snapshots from $t = 16,000$ to $20,000$ s are used for time average. This is because the oil droplets continue to rise after the bubbles are fully dissolved, causing the oil concentration field to take longer time to reach the statistically steady state within the sampling region (i.e., $0 \leq z \leq 400$ m).

Figure 8 shows the averaged gas mass dissolution rate α for the four cases with the gas dissolution effect modeled. Varying the initial bubble diameter induces two main effects. First, the bubbles with smaller initial diameter have smaller rise velocities and take longer time to rise through the same vertical distance than the larger bubbles. Second, smaller bubbles have higher surface area to volume ratio than larger bubbles. Therefore, with the same gas release rate, a case with a smaller bubble diameter would have a larger total effective bubble surface area than a case with larger bubbles, allowing for more efficient mass transfer through the bubble surfaces. As a result, the gas dissolution rate α is significantly high near the source for case QS-3D and becomes smaller as the initial bubble diameter increases to allow the bubbles survive over longer travel distance (Figure 8).

Figure 9 shows the contours of the mean bubble mass concentrations, in which the results for the cases with and without gas dissolution for the same initial bubble diameter are plotted side by side in each figure panel. Without considering the gas bubble dissolution, all the four simulation cases (i.e., QS-3N, QS-6N, QS-12N, and QS-18N) with different initial bubble diameters show similar structure for the mean bubble mass concentration (Figure 9): The bubble column extends continuously upward, and the local bubble mass concentration gradually decreases with height when the bubble column width expands due to the turbulent mixing and the radial flow motions associated with the peeling process. When the gas dissolution effect is considered in the LES, the height of the bubble column exhibits strong dependence on the initial bubble diameter due to the different gas dissolution rates shown in Figure 8. In particular, for cases QS-3D, QS-6D, QS-12D, and QS-18D, the corresponding height of the mean bubble column (based on the averaged bubble mass concentration) increases monotonically as around 50, 100, 190, and 280 m, respectively. Note that here, the height of the bubble column is estimated based on the bubble mass concentration due to its significance on determining the bubble-induced buoyancy. As shown later in Figure 14a, the individual gas bubbles can survive up to a higher elevation, where the bubbles have been dissolved to become too small to have noticeable effect on the plume dynamics (also see Figures 6a and 6b).

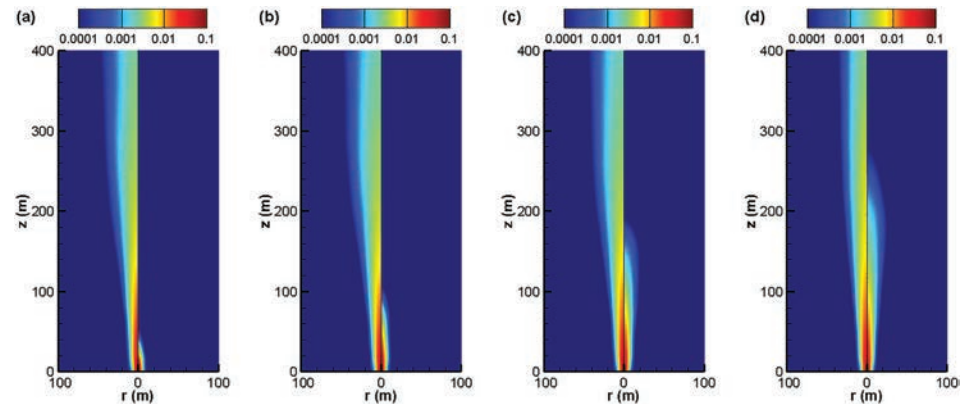


Figure 9. Time- and angular-averaged bubble mass concentration C_b (in kg/m^3): (a) cases Qs-3N (left half) and QS-3D (right half); (b) cases QS-6N (left half) and QS-6D (right half); (c) cases QS-12D (left half) and QS-12D (right half); (d) cases QS-18N (left half) and QS-18D (right half).

A more quantitative comparison of the mean gas bubble field between the cases with and without gas dissolution is shown in Figure 10, which shows the vertical distributions of the total gas bubble mass per unit depth obtained by horizontally averaging the mean bubble mass concentrations shown in Figure 9. With the gas dissolution effect considered, a plume with a smaller initial bubble diameter exhibits more rapid decay of the total bubble mass per depth in comparison to a plume with a larger initial bubble diameter. In contrast, the simulation results show an opposite trend if the gas dissolution is not considered, with the plumes of smaller bubbles exhibiting higher total bubble mass per depth than those with larger bubbles due to the accumulation of smaller bubbles with smaller rise velocity. This opposite trend for the four cases without gas dissolution is also not exactly monotonic (see cases QS-3N and QS-6N). Overall, the omission of the gas dissolution effect in the simulation result in unphysical concentration of gas bubbles continuously through the depth of the simulation domain.

Associated with the change of the bubble mass concentration, the peel height where the entrained seawater reaches the maximum elevation also varies significantly according to the initial bubble diameter. This can be seen from the contours of the mean vertical velocity of the plume shown in Figure 11. For case QS-3D, although the bubble mass concentration reduces to a negligible level above $z \approx 50$ m (Figure 9a), the plume

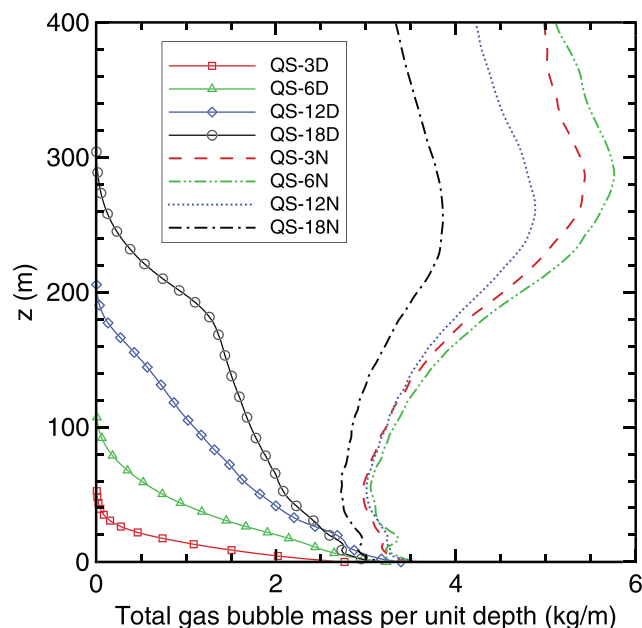


Figure 10. Vertical distribution of total gas bubble mass for the time- and angular-averaged plumes shown in Figure 9.

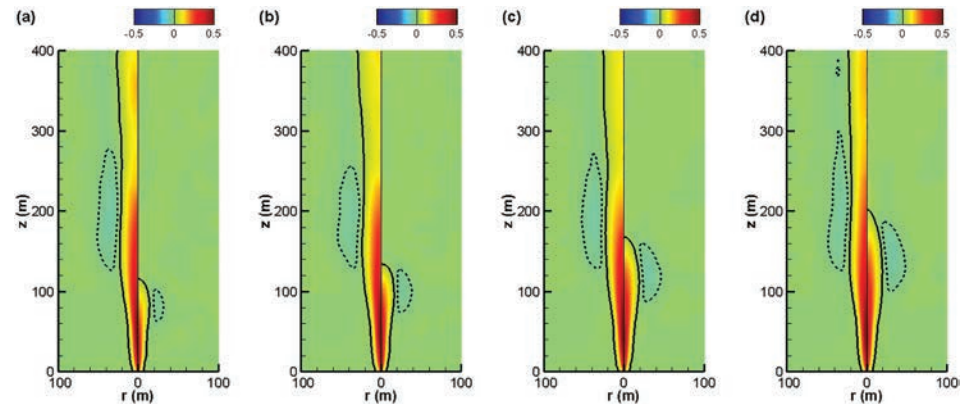


Figure 11. Time- and angular-averaged vertical velocity w (in m/s): (a) cases Qs-3N (left half) and Qs-3D (right half); (b) cases Qs-6N (left half) and Qs-6D (right half); (c) cases Qs-12D (left half) and Qs-12D (right half); (d) cases Qs-18N (left half) and Qs-18D (right half). The solid black lines indicate the contour lines of $w = 0.02$ m/s and the dashed black lines indicate the contour lines of $w = -0.02$ m/s.

flow has gained sufficient upward momentum and continues to rise to around $z \approx 120$ m (Figure 11a). At this maximum elevation, the entrained seawater with higher density than the local ambient seawater falls down along the outer plume around the inner plume, as indicated by the negative contours of the mean vertical velocity in Figure 11a. Similar situation occurs in case Qs-6D, for which the mean plume flow can reach around $z \approx 140$ m (Figure 11b) while the bubbles get dissolved to a negligible mass concentration level at a lower elevation of $z \approx 100$ m (Figure 9b). For case Qs-12D, the maximum elevation of the inner plume flow (i.e., the peel height) is at around $z \approx 170$ m (Figure 11c), which is slightly below the height of $z \approx 190$ m where the bubbles get fully dissolved (Figure 9c). For case Qs-18D, although the relatively low gas bubble dissolution rate allows the bubble column to reach around $z \approx 290$ m (Figure 9d), the continuous lifting of higher density seawater entrained from lower elevation as well as the reduction of bubble buoyancy due to gas dissolution cause the plume flow to slow down and peel at around $z \approx 200$ m (Figure 11d). As the initial bubble diameter increases, the four cases with gas dissolution effect exhibit an increase of intensity for the peeling process, as indicated by the increase of the outer plume size (see the negative vertical velocity contours in Figure 11). For all the four initial bubble diameters, the LES runs with the gas bubble dissolution effect considered show a significantly lower peel height than the corresponding LES runs without considering gas dissolution (i.e., the right half versus the left half in each panel of Figure 11).

Being affected by the dynamics of the plume, the concentration of the oil droplets also shows strong dependence on the initial bubble diameter (Figure 12). The oil droplets experience lateral dispersion away from the inner plume due to the turbulent mixing between the countercurrent inner and outer plumes as well as

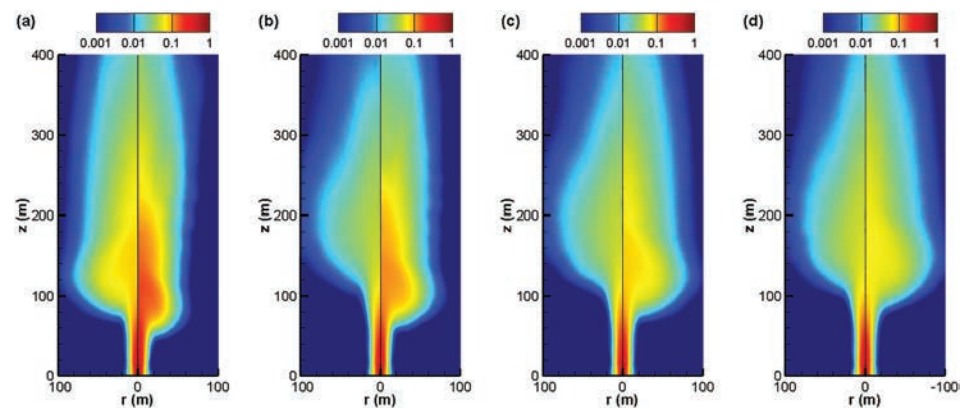


Figure 12. Time- and angular-averaged oil concentration \bar{C}_d (in kg/m^3): (a) cases Qs-3N (left half) and Qs-3D (right half); (b) cases Qs-6N (left half) and Qs-6D (right half); (c) cases Qs-12D (left half) and Qs-12D (right half); (d) cases Qs-18N (left half) and Qs-18D (right half).

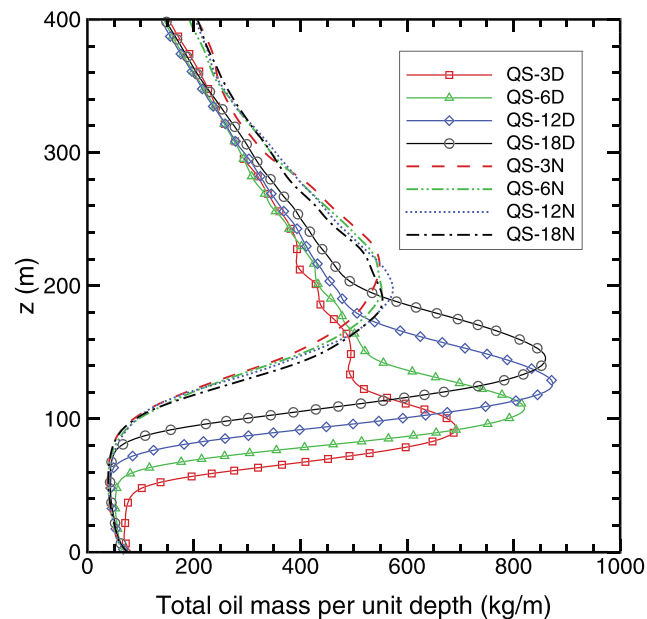


Figure 13. Vertical distribution of total oil droplet mass for the time- and angular-averaged plumes shown in Figure 12.

the lateral flow motions of the peeling process (see Figures 6g and 6h). In the four cases with gas bubble dissolution modeled, the oil droplets eventually escape from the inner and outer plumes and continue to rise by their own buoyancy, without further experiencing significant lateral dispersion above the peel height. As shown in Figure 12, for the four simulation cases with gas dissolution effect, the oil concentrations are more diluted and laterally spread in the cases with larger initial bubble size. For example, in case QS-3D (Figure 12a), the upward plume flow is weak and has limited vertical extension due to the rapid dissolution of the small gas bubbles, which results in weak turbulent entrainment and peeling process for lateral oil dispersion. In case QS-18D (Figure 12d), the large bubbles induce strong inner/outer plumes and peeling process to help disperse the oil droplets laterally away from the inner plume and dilute the oil concentration. In contrast, when the gas dissolution effect is not considered, the simulation results for all the four initial bubble diameters show significantly more dilution of the oil concentration compared to the corresponding simulation cases with the gas dissolution effect considered. The overall oil transport process is dominated by the effect of the continuously rising bubble column without the proper gas dissolution effect being included.

For a more quantitative comparison of the plumes of 0.5 mm oil droplets, the mean oil droplet mass concentrations of the eight cases shown in Figure 12 are integrated horizontally to obtain the vertical distributions of the total oil droplet mass per unit depth. Figure 13 compares results for the cases with and without the gas bubble dissolution. For each vertical profile of the oil droplet mass distribution, there exists a distinct peak corresponding to the height of the intrusion layer. If the gas dissolution effect is included, the intrusion layer shift upwards as the initial bubble diameter increases because of the higher maximum elevation that the gas bubble column that the reach before full dissolution. Specifically, the oil intrusion layer is located at $z \approx 94$ m for case QS-3D, at $z \approx 107$ m for case QS-6D, at $z \approx 127$ m for case QS-12D, and at $z \approx 147$ m for case QS-18D. The omission of the gas dissolution effect in the simulation causes consistent overestimation of the oil plume intrusion layer for the plumes with all the four different initial bubble diameters, that is, $z \approx 214$ m for case QS-3N, $z \approx 197$ m for case QS-6N, $z \approx 197$ m for case QS-12N, and $z \approx 190$ m for case QS-18N. Overall, the relative error is in the range of 30%–127%, with larger relative error for the cases with smaller initial bubble diameter.

Several mean plume properties can also be calculated based on the smooth flow and scalar quantity fields of the time- and angular-averaged plume to show the vertical variation of the mean plume characteristics under the influence of gas bubble dissolution. Figure 14a shows the vertical variation of the mean bubble diameter (normalized by the corresponding initial bubble diameter). Consistent with the time- and angular-averaged gas bubble dissolution rate (Figure 8), the cases with smaller initial bubble diameters show more rapid decrease of the mean bubble diameter with height than the cases with larger initial bubble diameters.

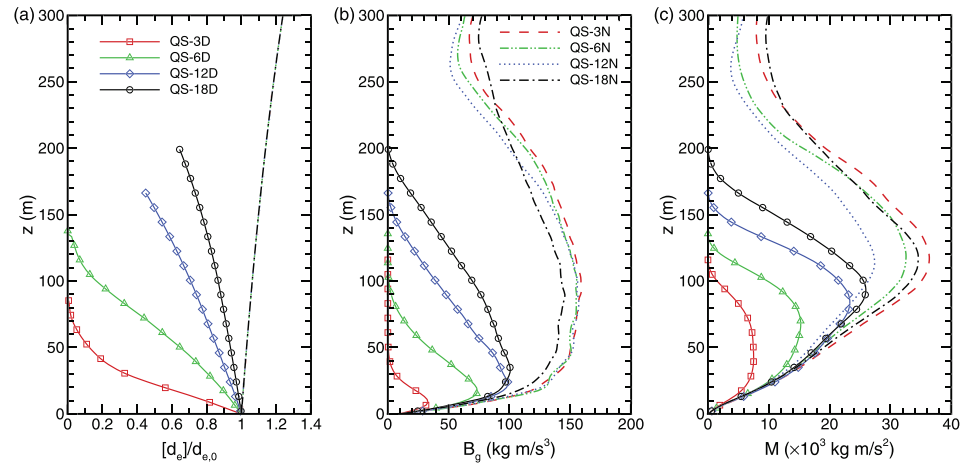


Figure 14. Averaged inner plume statistics: (a) mean bubble diameter (normalized by the initial bubble diameter); (b) bubble-induced buoyancy flux; (c) momentum flux of inner plume carrier flow. In each panel, the solid lines with different symbols are for the cases with gas dissolution effect, and the lines without symbols are for the reference cases without gas dissolution effect.

The reduction of the bubble size causes the bubble-induced buoyancy flux in the inner plume to reduce continuously as the plume rises. The mean buoyancy flux of the gas bubbles can be calculated as

$$B_g = \int_0^{b_i} \left(\frac{\rho_0}{\rho_b} - 1 \right) \langle \tilde{C}_b \rangle \langle \tilde{w} \rangle g 2\pi r dr. \quad (34)$$

Figure 14b shows the vertical variation of the bubble-induced buoyancy flux B_g in the inner plume. For all the simulation cases, near the source of release the magnitude of B_g increases with height due to the initial acceleration of the vertical plume velocity $\langle \tilde{w} \rangle$ and the accumulated bubble concentration $\langle \tilde{C}_b \rangle$. As the elevation further increases, for the cases with bubble gas dissolution considered, B_g decreases rapidly as the bubbles get dissolved. For cases QS-3D and QS-6D, B_g reduces to a negligible level at around $z = 50$ and 100 m, respectively. These heights are consistent with the maximum heights of the mean bubble mass concentration contours shown in Figures 9a and 9b. For cases QS-12D and QS-18D, B_g reduces to zero at around $z = 170$ and 200 m, respectively, where the corresponding bubble concentration $\langle \tilde{C}_b \rangle$ is still significant but the plume vertical velocity $\langle \tilde{w} \rangle$ has reduced to zero and the peeling process occurs. Comparison among the four cases with gas dissolution effect shows that the magnitude of B_g increases monotonically as the initial bubble diameter increases due to the effect of the monotonic decrease of gas bubble dissolution rate α shown in Figure 8.

The response of the plume flow to the variation of bubble buoyancy and seawater stratification can be seen from Figure 14c based on the mean momentum flux,

$$M = \int_0^{b_i} \langle \tilde{\rho} \rangle \langle \tilde{w} \rangle^2 2\pi r dr. \quad (35)$$

For the four cases with gas dissolution effect, several characteristic quantities of the plume momentum flux (including the magnitude, the peak height, and the height where the flux reduces to zero) increase monotonically as the initial bubble diameter increases due to the increase of the bubble buoyancy that drives the plume motion. For the four cases with the gas dissolution effect considered, Figure 14 shows that the mean plume peel height (where M reduces to zero) is at $z \approx 115$ m for case QS-3D, at $z \approx 135$ m for case QS-6D, at $z \approx 165$ m for case QS-12D, and at $z \approx 200$ m for case QS-18D. In contrast, the omission of the gas bubble dissolution effect results in a consistent overestimation of the mean plume peel height (at $z \in (250, 300)$ m where M reaches a local minimum) for the four cases without considering the gas bubble dissolution, that is, at $z \approx 289$ m for case QS-3N, at $z \approx 285$ m for case QS-6N, at $z \approx 260$ m for case QS-12N, and at $z \approx 284$ m for case QS-18N. Overall, the relative error for the estimated mean plume peel height due to the omission of the gas bubble dissolution effect is in the range of 42%–151% for the reported cases, with larger relative error for cases with smaller initial bubble diameter.

The above results illustrate that the current LES plume gas dissolution model can capture the key effects of the gas dissolution on the dynamics and structures of the plume. In contrast, if the gas bubble dissolution effect is not included in the model, the bubble diameter expands with height simply due to the reduction of the hydrostatic pressure in the seawater (Figure 14a). The persistence of the bubble-induced buoyancy as the plume rises (Figure 14b) results in overprediction of the plume momentum flux for all the four initial bubble diameters considered in this study (Figure 14c), causing inaccurate prediction of the plume peel height and other key plume characteristics as shown in Figures 7 and 9–12.

5. Conclusion

In the case of a subsea blowout event, the dynamics of the near-field plume is highly affected by the buoyancy provided by the gas bubbles. In the deep-water environment, the gas in the bubbles dissolves continuously into the surrounding seawater, causing the plume to lose its driving force during the rising process. Thus, it is crucial to account for the effect of gas bubble dissolution in order to model the dynamics and structure of the near-field plume properly. In this study, an Eulerian-Eulerian LES modeling strategy has been developed to model the effect of gas dissolution on the dynamics of the multiphase near-field plume. In particular, the model parameterizes the local gas dissolution rate within each computational cell based on the instantaneous local Eulerian gas mass concentration and bubble number density functions obtained from the LES. The modeled gas dissolution rate is then included in the transport equation of the gas mass concentration to account for the loss of bubble mass due to the dissolution of gas into the surrounding seawater. This Eulerian-Eulerian LES modeling strategy provides a cost-efficient approach to incorporate the important gas dissolution effect into the simulation of field-scale plumes consisting of a large number of dispersed gas bubbles.

In this study, the LES model is applied to simulate the multiphase hydrocarbon plume released from the 700-m depth driven by methane bubbles, with four different initial bubble diameters being considered under identical volumetric release rate. Due to the increase of the total surface area to volume ratio as the initial bubble diameter is reduced, the cases with smaller initial bubble diameters experience faster gas dissolution than those cases with larger initial diameters. The new LES model is found to be able to successfully model the bubble dissolution and capture its effect on the plume dynamics. The LES results show that several key physical quantities of the plume, such as the maximum height of the bubble column, the peel height of the plume entrained fluid, as well as the magnitudes of the plume buoyancy and momentum fluxes, all increase monotonically as the initial bubble diameter increases for the cases considered in this study. In contrast, a set of reference LES runs without considering the gas dissolution effect fail to capture the proper trend for the variations in the structure of the plume with different initial bubble diameters, indicating the importance of properly including the gas dissolution effect for an accurate prediction of the near-field plume dynamics in subsea blowouts.

Appendix A: Peng-Robinson Equation of State for Nonideal Gas

Following Sloan (1997) and Zheng and Yapa (2002), under the deep-water environment, the gas in the bubbles is assumed to behave as nonideal gas. The state of the nonideal gas can be modeled using the Peng-Robinson equation (Peng & Robinson, 1976),

$$p_b = \frac{RT}{V_m - b} - \frac{a}{V_m(V_m + b) + b(V_m - b)}, \quad (\text{A1})$$

where V_m is the gas molar volume and a and b are model coefficients. For bubbles with a single gas component, a and b can be modeled as

$$a(T) = a(T_c) \beta(T_r, \omega), \quad (\text{A2})$$

$$b(T) = b(T_c). \quad (\text{A3})$$

where T is the temperature, T_c is the critical temperature,

$$a(T_c) = 0.45724 \frac{R^2 T_c^2}{P_c^2}, \quad (\text{A4})$$

$$b(T_c) = 0.07780 \frac{RT_c}{P_c}, \quad (\text{A5})$$

and P_c is the critical pressure. In case if the state of bubbles with multiple gas components is to be modeled, the calculations of a and b need to be modified by including the gas mixture parameters for different gas components (Peng & Robinson, 1976).

In Equation A2, $\beta(T_r, \omega)$ is a dimensionless function of the reduced temperature T_r and acentric factor ω (Peng & Robinson, 1976; Soave, 1972),

$$\beta^{1/2} = 1 + \kappa(\omega) (1 - T_r^{1/2}), \quad (\text{A6})$$

where $T_r = 0.7$ and

$$\kappa(\omega) = 0.37464 + 1.54226\omega - 0.26992\omega^2. \quad (\text{A7})$$

In this study, we consider the dissolution of methane bubbles, for which the corresponding values of the above modeling parameters are $T_c = 190.4$ K, $P_c = 4.6 \times 10^6$ Pa, and $\omega = 0.011$ (Reid et al., 1987).

Equation A1 can be rewritten in polynomial form as (Peng & Robinson, 1976)

$$Z^3 - (1 - B)Z^2 + (A - 2B^2 - 3B^2) - (AB - B^2 - B^3) = 0, \quad (\text{A8})$$

where

$$A = \frac{ap_b}{R^2 T^2}, \quad (\text{A9})$$

$$B = \frac{bp_b}{RT}, \quad (\text{A10})$$

$$Z = \frac{p_b V_m}{RT}. \quad (\text{A11})$$

By solving Equation A8, the compressibility factor Z can be obtained and used in the model equations 3-5 and 14.

Appendix B: Terminal Velocity of a Single Bubble

Following the modeling approach in Zheng and Yapa (2000) and Zhao et al. (2016a), in the current study the bubble rise velocity $w_{r,b}$ relative to the surrounding fluid flow is modeled based on the equivalent spherical diameter d_e using the parameterizations from Clift et al. (1978). In particular, for the small spherical bubbles with $d_e \leq 1$ mm (Zheng & Yapa, 2000), the rise velocity is parameterized based on the particle Reynolds number $\text{Re}_b = \rho_0 w_{r,b} d_e / \mu$, where ρ_0 and μ are the density and dynamic viscosity of the water, respectively. By reversing the definition of Reynolds number, one obtains (Zheng & Yapa, 2000)

$$w_{r,b} = \frac{\text{Re}_b \mu}{\rho_0 d_e}, \quad (\text{B1})$$

in which Re_b can be parameterized in explicit function form as (Clift et al., 1978)

$$\left\{ \begin{array}{ll} \text{Re}_b = N_D/24 - 1.7569 \times 10^{-4} N_D^2 \\ \quad + 6.9252 \times 10^{-7} N_D^3 \\ \quad - 2.3027 \times 10^{-10} N_D^4, & \text{if } N_D \leq 73, \\ \log_{10} \text{Re}_b = -1.7095 + 1.33438W - 0.11591W^2, & \text{if } 72 < N_D \leq 580, \\ \log_{10} \text{Re}_b = -1.81391 + 1.34671W - 0.12427W^2 \\ \quad + 0.006344W^3, & \text{if } 580 < N_D \leq 1.55 \times 10^7, \end{array} \right. \quad (\text{B2})$$

where $N_D = 4\rho_0(\rho_0 - \rho_b)gd_e^3/3\mu^2$ and $W = \log_{10}N_D$.

As the bubble diameter increases, the bubble shape becomes the ellipsoidal shape for the intermediate size regime and the spherical-cap shape for the large size regime, with the two regimes separated by a critical bubble diameter d_{cr} (Clift et al., 1978; Zheng & Yapa, 2000). For the ellipsoidal bubbles with $1 \text{ mm} < d_e \leq d_{cr}$, the bubble rise velocity is modeled as (Clift et al., 1978)

$$w_{r,b} = \frac{\mu}{\rho_0 d_e} M^{-0.149} J - 0.857, \quad (\text{B3})$$

where $M = g\mu^4(\rho_0 - \rho_b)/\rho_0^2\sigma^3$ is the Morton number and J is a general correlation,

$$J = \begin{cases} 0.94h^{0.757}, & \text{if } 2 < h \leq 59.3, \\ 3.42h^{0.411}, & \text{if } h > 59.3. \end{cases} \quad (\text{B4})$$

Here, h is given by

$$h = \frac{4}{3} Eo M^{-0.149} \left(\frac{\mu}{\mu_*} \right)^{-0.14}, \quad (\text{B5})$$

where $\mu_* = 9 \times 10^{-4} \text{ kg/(m s)}$ is a reference dynamic viscosity of water (Grace, 1976). For the spherical-cap shape bubbles with $d_e > d_{cr}$, the rise velocity is modeled as (Clift et al., 1978)

$$w_{r,b} = 0.711 \sqrt{gd_e(\rho_0 - \rho_b)/\rho_0}. \quad (\text{B6})$$

The critical diameter d_{cr} that separates the ellipsoidal and spherical-cap shape regimes of the bubble rise velocity parameterization may be determined based on the criterion $Eo = 40$ (Clift et al., 1978; Zheng & Yapa, 2000). Zheng and Yapa (2000) pointed out that this approach would result in the parameterization of $w_{r,b}$ being discontinuous near d_{cr} . They proposed to determine d_{cr} by finding the intersection of the two lines that represent Equations B3 and B6, which has also been used by Zhao et al. (2016a). Applying the approach of Zheng and Yapa (2000) to the plume conditions considered in the current study yields a critical bubble diameter of about $d_{cr} = 10 \text{ mm}$, which is used for determining the applicable regimes of Equations B3 and B6.

Appendix C: Summary of the LES Model's Solution Process and Numerical Schemes

The current LES modeling framework involves a number of equations describing the motions of the plume flow as well as the transport of scalar quantities. This appendix highlights the process for solving the LES model's equations. Details of the model equations can be found in section 2.

The solution process for advancing the plume flow and scalar fields forward for one time step in the LES model is summarized as follows:

- (a) At the beginning of each time step, the cell-averaged number of moles of gas per bubble, n_b , is computed based on Equation 2 using the bubble mass concentration \tilde{C}_b and number density \tilde{N}_b available at the current time step. The three Boussinesq buoyancy terms in Equation 17 are also calculated based on the corresponding scalar values at the current time step.
- (b) The equivalent diameter d_e for the cell-averaged bubble size is calculated using Equation 4 based on n_b obtained from Step (a).
- (c) The corresponding gas mass transfer coefficient K is calculated using Equations 6, 7, 9, and 10 for different bubble diameter regimes.
- (d) The cell-averaged value of the single bubble dissolution rate α_b is modeled based on Equations 11–15, and the bubble mass dissolution rate per volume for a local LES cell, $\tilde{\alpha}$, is calculated based on Equation 23.
- (e) The gas-related transport equations 20, 22, and 24 are integrated in time based on the modeled gas dissolution rate $\tilde{\alpha}$, with the bubble rise velocity in Equation 21 being parameterized based on the equivalent bubble diameter d_e using Equations B1, B3, and B6. The bubble number density \tilde{N}_b and mass concentration \tilde{C}_b as well as the dissolved gas mass concentration \tilde{C}_{dis} are updated to a new time step.
- (f) The LES scalar transport equations 18, 25, and 26 are integrated in time and the corresponding scalar fields $\tilde{\theta}$, $\tilde{\rho}$, \tilde{C}_{dye} and \tilde{C}_d are updated to a new time step.

- (g) The LES carrier flow equations 16 and 17 are advanced in time with the Boussinesq buoyancy terms calculated in Step (a), and the carrier flow velocity $\tilde{\mathbf{u}}$ is updated to the new time step.

The solution process summarized above is repeated in every time step to advance the entire plume simulation forward in time. The current LES model uses a hybrid scheme for simulating the flow and scalar field evolutions. For the flow field, Equations 16–18 are discretized by the pseudo-spectral method in the horizontal directions on collocated grids and the second-order central finite difference method in the vertical direction on staggered grids (Albertson & Parlange, 1999). The velocity field is advanced in time by a fractional-step method, including a velocity prediction step that integrates Equation 17 by the second-order Adams-Bashforth scheme, and a pressure correction step by constructing and solving a pressure Poisson equation based on the divergence-free constraint Equation 16 to project the predicted velocity field onto the divergence-free space. Equation 18 is also integrated in time by the second-order Adams-Bashforth scheme. The transport equations 20, 22, and 24–26 for the spatially nonhomogeneous concentration fields are discretized by a finite-volume method, which uses the carrier flow velocity field interpolated from the pseudo-spectral/finite-difference flow solver's computational grids to the finite-volume grids using a constrained interpolation scheme that conserves the velocity divergence-free condition (Chamecki et al., 2008). The LES solver for these transport equations uses a bounded third-order upwind scheme for the advection term (Gaskell & Lau, 1988) and advances the concentration fields in time using the second-order Adams-Bashforth scheme (Chamecki et al., 2008).

Data Availability Statement

The data associated with this paper are publicly available through the Gulf of Mexico Research Initiative Information and Data Cooperative (GRIIDC) at <https://data.gulfresearchinitiative.org/data/R5.x283.277:0001> (doi: 10.7266/n7-5bp2-m135).

Acknowledgments

This research was made possible by a grant from The Gulf of Mexico Research Initiative. The authors are grateful to Charles Meneveau and Marcelo Chamecki for insightful discussions on the development of the LES model. The authors also acknowledge the financial support from DY's start-up funds, the technical support on computer hardware from the Research Computing Center (RCC), and the use of computational resource from the Research Computing Data Core (RCDC) at the University of Houston for conducting the simulations presented in this paper.

References

- Aiyer, A. K., Yang, D., Chamecki, M., & Meneveau, C. (2019). A population balance model for large eddy simulation of polydisperse droplet evolution. *Journal of Fluid Mechanics*, *878*, 700–739. <https://doi.org/10.1017/jfm.2019.649>
- Albertson, J. D., & Parlange, M. B. (1999). Surface length scales and shear stress: Implications for land-atmosphere interaction over complex terrain. *Water Resource Research*, *35*(7), 2121–2132. <https://doi.org/10.1029/1999WR900094>
- Antonopoulos-Domis, M. (1981). Large-eddy simulation of a passive scalar in isotropic turbulence. *Journal of Fluid Mechanics*, *104*, 55–79. <https://doi.org/10.1017/S0022112081002814>
- Asaeda, T., & Imberger, J. (1993). Structure of bubble plumes in linearly stratified environments. *Journal of Fluid Mechanics*, *249*, 35–57. <https://doi.org/10.1017/S0022112093001065>
- Bou-Zeid, E., Meneveau, C., & Parlange, M. B. (2005). A scale-dependent Lagrangian dynamic model for large eddy simulation of complex turbulent flows. *Physics of fluids*, *17*(2), 25,105. <https://doi.org/10.1063/1.1839152>
- Camilli, R., Di Iorio, D., Bowen, A., Reddy, C. M., Techet, A. H., Yoerger, D. R., et al. (2012). Acoustic measurement of the Deepwater Horizon Macondo well flow rate. *Proceedings of the National Academy of Sciences*, *109*(50), 20,235–20,239. <https://doi.org/10.1073/pnas.1100385108>
- Carroll, J. (1993). Use Henry's law for multicomponent mixtures. *Chemical Engineering Progress*, *88*(8), 53–58.
- Carroll, J. J., & Mather, A. E. (1997). A model for the solubility of light hydrocarbons in water and aqueous solutions of alkanolamines. *Chemical Engineering Science*, *52*(4), 545–552. [https://doi.org/10.1016/S0009-2509\(96\)00437-X](https://doi.org/10.1016/S0009-2509(96)00437-X)
- Chamecki, M., Meneveau, C., & Parlange, M. B. (2008). A hybrid spectral/finite-volume algorithm for large-eddy simulation of scalars in the atmospheric boundary layer. *Boundary-Layer Meteorology*, *128*(3), 473–484. <https://doi.org/10.1007/s10546-008-9302-1>
- Chamecki, M., Meneveau, C., & Parlange, M. B. (2009). Large eddy simulation of pollen transport in the atmospheric boundary layer. *Journal of Aerosol Science*, *40*(3), 241–255. <https://doi.org/10.1016/j.jaerosci.2008.11.004>
- Chan, G. K. Y., Chow, A. C., & Adams, E. E. (2015). Effects of droplet size on intrusion of sub-surface oil spills. *Environmental Fluid Mechanics*, *15*, 959–973. <https://doi.org/10.1007/s10652-014-9389-5>
- Chen, B., Yang, D., & Meneveau, C. (2016). Effects of swell on transport and dispersion of oil plumes within the ocean mixed layer. *Journal of Geophysical Research: Oceans*, *121*, 3564–3578. <https://doi.org/10.1002/2015JC011380>
- Chen, B., Yang, D., Meneveau, C., & Chamecki, M. (2018). Numerical study of the effects of chemical dispersant on oil transport from an idealized underwater blowout. *Physical Review Fluids*, *3*(6), 64,501. <https://doi.org/10.1103/PhysRevFluids.3.083801>
- Chen, F., & Yapa, P. (2003). D A model for simulating deep water oil and gas blowouts—Part II: Comparison of numerical simulations with “Deepspill” field experiments. *Journal of Hydraulic Research*, *41*(4), 353–365. <https://doi.org/10.1080/00221680309499981>
- Chor, T., Yang, D., Meneveau, C., & Chamecki, M. (2018). Preferential concentration of noninertial buoyant particles in the ocean mixed layer under free convection. *Physical Review Fluids*, *3*(8), 83,801. <https://doi.org/10.1103/PhysRevFluids.3.064501>
- Clift, R., & Gauvin, W. H. (1971). Motion of entrained particles in gas streams. *The Canadian Journal of Chemical Engineering*, *49*(4), 439–448. <https://doi.org/10.1002/cjce.5450490403>
- Clift, R. G., Grace, J. R., & Weber, M. E. (1978). *Bubbles, drops, and particles*. New York, NY: Academic Press.
- Crouse, B. C., Wannamaker, E. J., & Adams, E. E. (2007). Integral model of a multiphase plume in quiescent stratification. *Journal of Hydraulic Engineering*, *133*(1), 70–76. [https://doi.org/10.1061/\(ASCE\)0733-9429\(2007\)133:1\(70\)](https://doi.org/10.1061/(ASCE)0733-9429(2007)133:1(70))
- Deen, N. G., Solberg, T., & Hjertager, B. H. (2001). Large eddy simulation of the gas–liquid flow in a square cross-sectioned bubble column. *Chemical engineering science*, *56*(21–22), 6341–6349. [https://doi.org/10.1016/S0009-2509\(01\)00249-4](https://doi.org/10.1016/S0009-2509(01)00249-4)

- Dhotre, M. T., Deen, N. G., Niceno, B., Khan, Z., & Joshi, J. (2013). B Large eddy simulation for dispersed bubbly flows: A review. *International Journal of Chemical Engineering*, 2013, 343,276. <https://doi.org/10.1155/2013/343276>
- Dissanayake, A. L., Gros, J., & Socolofsky, S. A. (2018). Integral models for bubble, droplet, and multiphase plume dynamics in stratification and crossflow. *Environmental Fluid Mechanics*, 18(5), 1167–1202. <https://doi.org/10.1007/s10652-018-9591-y>
- Fabregat, A., Dewar, W. K., Özgökmen, T. M., Poje, A. C., & Wienders, N. (2015). Numerical simulations of turbulent thermal, bubble and hybrid plumes. *Ocean Modelling*, 90, 16–28. <https://doi.org/10.1016/j.ocemod.2015.03.007>
- Fabregat Tomàs, A., Poje, A. C., Özgökmen, T. M., & Dewar, W. K. (2016). Dynamics of multiphase turbulent plumes with hybrid buoyancy sources in stratified environments. *Physics of Fluids*, 28(9), 95,109. <https://doi.org/10.1063/1.4963313>
- Ferry, J., & Balachandar, S. (2001). A fast Eulerian method for disperse two-phase flow. *International Journal of Multiphase Flow*, 27(7), 1199–1226. [https://doi.org/10.1016/S0301-9322\(00\)00069-0](https://doi.org/10.1016/S0301-9322(00)00069-0)
- Fraga, B., Stoesser, T., Lai, C. C. K., & Socolofsky, S. A. (2016). A LES-based Eulerian–Lagrangian approach to predict the dynamics of bubble plumes. *Ocean modelling*, 97, 27–36. <https://doi.org/10.1016/j.ocemod.2015.11.005>
- Fraga, B., & Stoesser, T. (2016). Influence of bubble size, diffuser width, and flow rate on the integral behavior of bubble plumes. *Journal of Geophysical Research: Oceans*, 121, 3887–3904. <https://doi.org/10.1002/2015JC011381>
- Frössling, N. (1938). Über die Verdunstung fallender Tropfen. *Gerlands Beiträge zur Geophysik*, 52, 170–216.
- Gaskell, P. H., & Lau, A. K. C. (1988). *Curvature-compensated convective transport: SMART, A new boundedness-preserving transport algorithm*. *International Journal for Numerical Methods in Fluids*, 8(6), 617–641. <https://doi.org/10.1002/flid.1650080602>
- Grace, J. R. (1976). Shapes and velocities of single drops and bubbles moving freely through immiscible liquids. *Chemical Engineering Research and Design*, 54, 167–173.
- Gros, J., Reddy, C. M., Nelson, R. K., Socolofsky, S. A., & Arey, J. S. (2016). Simulating gas–liquid–water partitioning and fluid properties of petroleum under pressure: Implications for deep-sea blowouts. *Environmental Science & Technology*, 50(14), 7397–7408. <https://doi.org/10.1021/acs.est.5b04617>
- Gros, J., Socolofsky, S. A., Dissanayake, A. L., Jun, I., Zhao, L., Boufadel, M. C., et al. (2017). Petroleum dynamics in the sea and influence of subsea dispersant injection during Deepwater Horizon. *Proceedings of the National Academy of Sciences*, 114(38), 10,065–10,070. <https://doi.org/10.1073/pnas.1612518114>
- Hu, G., & Celik, I. (2008). Eulerian–Lagrangian based large-eddy simulation of a partially aerated flat bubble column. *Chemical Engineering Science*, 63(1), 253–271. <https://doi.org/10.1016/j.ces.2007.09.015>
- King, M. B. (1969). *Phase Equilibrium in Mixtures Oxford*. UK: Pergamon Press.
- Kukulka, T., Plueddemann, A. J., Trowbridge, J. H., & Sullivan, P. (2010). P Rapid mixed layer deepening by the combination of Langmuir and shear instabilities: A case study. *Journal of Physical Oceanography*, 40(11), 2381–2400. <https://doi.org/10.1175/2010JPO4403.1>
- Kumar, V., Kleissl, J., Meneveau, C., & Parlange, M. (2006). B Large-eddy simulation of a diurnal cycle of the atmospheric boundary layer: Atmospheric stability and scaling issues. *Water resources research*, 42, W06D09. <https://doi.org/10.1029/2005WR004651>
- Lai, C., & Socolofsky, S. (2019). The turbulent kinetic energy budget in a bubble plume. *Journal of Fluid Mechanics*, 865, 993–1041. <https://doi.org/10.1017/jfm.2019.66>
- Lekvam, K., & Bishnoi, P. R. (1997). Dissolution of methane in water at low temperatures and intermediate pressures. *Fluid Phase Equilibria*, 131(1-2), 297–309. [https://doi.org/10.1016/S0378-3812\(96\)03229-3](https://doi.org/10.1016/S0378-3812(96)03229-3)
- Lemckert, C. J., & Imberger, J. (1993). Energetic bubble plumes in arbitrary stratification. *Journal of Hydraulic Engineering*, 119(6), 680–703. [https://doi.org/10.1061/\(ASCE\)0733-9429\(1993\)119:6\(680\)](https://doi.org/10.1061/(ASCE)0733-9429(1993)119:6(680))
- Liang, J.-H., McWilliams, J. C., Sullivan, P. P., & Baschek, B. (2012). Large eddy simulation of the bubbly ocean: New insights on sub-surface bubble distribution and bubble-mediated gas transfer. *Journal of Geophysical Research*, 117, C04002. <https://doi.org/10.1029/2011JC007766>
- Lilly, D. K. (1967). The representation of small-scale turbulence in numerical simulation experiments. Yorktown Heights: NY.
- Mason, P. J., & Journal of the Atmospheric Sciences (1989). Large-eddy simulation of the convective atmospheric boundary layer, 46(11), 1492–1516. [https://doi.org/10.1175/1520-0469\(1989\)046<1492:LESOTC>2.0.CO;2](https://doi.org/10.1175/1520-0469(1989)046<1492:LESOTC>2.0.CO;2)
- McNutt, M. K., Camilli, R., Crone, T. J., Hsieh, P. A., Ryerson, T. B., Savas, O., & Shaer, F. (2012). Review of flow rate estimates of the Deepwater Horizon oil spill. *Proceedings of the National Academy of Sciences*, 109(50), 20,260–20,267. <https://doi.org/10.1073/pnas.1112139108>
- McWilliams, J. C., Sullivan, P. P., & Moeng, C.-H. (1997). Langmuir turbulence in the ocean. *Journal of Fluid Mechanics*, 334, 1–30. <https://doi.org/10.1017/S0022112096004375>
- Moeng, C.-H. (1984). A large-eddy simulation model for the study of planetary boundary-layer turbulence. *Journal of the Atmospheric Sciences*, 41(13), 2052–2062. [https://doi.org/10.1175/1520-0469\(1984\)041<2052:ALESMF>2.0.CO;2](https://doi.org/10.1175/1520-0469(1984)041<2052:ALESMF>2.0.CO;2)
- Motarjemi, M., & Jameson, G. J. (1978). Mass transfer from very small bubbles—The optimum bubble size for aeration. *Chemical Engineering Science*, 33(11), 1415–1423. [https://doi.org/10.1016/0009-2509\(78\)85190-2](https://doi.org/10.1016/0009-2509(78)85190-2)
- Murphy, D. W., Xue, X., Sampath, K., & Katz, J. (2016). Crude oil jets in crossflow: Effects of dispersant concentration on plume behavior. *Journal of Geophysical Research: Oceans*, 121, 4264–4281. <https://doi.org/10.1002/2015JC011574>
- Peng, D. Y., & Robinson, D. B. (1976). A new two-constant equation of state. *Industrial and Engineering Chemistry Fundamentals*, 15(1), 59–64. <https://doi.org/10.1021/i160057a011>
- Polton, J. A., Smith, J. A., MacKinnon, J. A., & Tejada-Martinez, A. E. (2008). Rapid generation of high-frequency internal waves beneath a wind and wave forced oceanic surface mixed layer. *Geophysical Research Letters*, 35, L13602. <https://doi.org/10.1029/2008GL038356>
- Reddy, C. M., Arey, J. S., Seewald, J. S., Sylva, S. P., Lemkau, K. L., Nelson, R. K., et al. (2012). Composition and fate of gas and oil released to the water column during the Deepwater Horizon oil spill. *Proceedings of the National Academy of Sciences*, 109, 20,229–20,234. <https://doi.org/10.1073/pnas.1101242108>
- Reid, R. C., Prausnitz, J. M., & Poling, B. E. (1987). *The properties of gases and liquids* (4th Ed.). New York, NY: McGraw-Hill.
- Richards, T. S., Aubourg, Q., & Sutherland, B. R. (2014). Radial intrusions from turbulent plumes in uniform stratification. *Physics of Fluids*, 3, 36,602. <https://doi.org/10.1063/1.4869119>
- Scala, F. (2011). Mass transfer around active particles in fluidized beds, *Mass Transfer in Multiphase Systems and its Applications (Chap 25 pp. 571–592)*: Croatia.
- Seol, D.-G., Bryant, D. B., & Socolofsky, S. A. (2009). Measurement of behavioral properties of entrained ambient water in a stratified bubble plume. *Journal of Hydraulic Engineering*, 135(11), 983–988. [https://doi.org/10.1061/\(ASCE\)HY.1943-7900.0000109](https://doi.org/10.1061/(ASCE)HY.1943-7900.0000109)
- Sloan, E. D. Jr. (1997). *Clathrate hydrates of natural gases* (2nd ed.). New York, NY: Marcel Dekker.
- Smagorinsky, J. (1963). General circulation experiments with the primitive equations. I: The basic experiment. *Monthly Weather Review*, 91(3), 99–164. [https://doi.org/10.1175/1520-0493\(1963\)091<0099:GCEWTP>2.3.CO;2](https://doi.org/10.1175/1520-0493(1963)091<0099:GCEWTP>2.3.CO;2)

- Soave, G. (1972). Equilibrium constants from a modified Redlich–Kwong equation of state. *Chemical Engineering Science*, 27(6), 1197–1203. [https://doi.org/10.1016/0009-2509\(72\)80096-4](https://doi.org/10.1016/0009-2509(72)80096-4)
- Socolofsky, S. A., & Adams, E. E. (2003). Liquid volume fluxes in stratified multiphase plumes. *Journal of Hydraulic Engineering*, 129(11), 905–914. [https://doi.org/10.1061/\(ASCE\)0733-9429\(2003\)129:11\(905\)](https://doi.org/10.1061/(ASCE)0733-9429(2003)129:11(905))
- Socolofsky, S. A., & Adams, E. E. (2005). Role of slip velocity in the behavior of stratified multiphase plumes. *Journal of Hydraulic Engineering*, 131(4), 273–282. [https://doi.org/10.1061/\(ASCE\)0733-9429\(2005\)131:4\(273\)](https://doi.org/10.1061/(ASCE)0733-9429(2005)131:4(273))
- Socolofsky, S. A., Adams, E. E., Paris, C., & Yang, D. (2016). How do oil, gas, and water interact near a subsea blowout? *Oceanography*, 29, 64–75. <https://doi.org/10.5670/oceanog.2016.63>
- Socolofsky, S. A., Adams, E. E., & Sherwood, C. R. (2011). Formation dynamics of subsurface hydrocarbon intrusions following the Deepwater Horizon blowout. *Geophysical Research Letters*, 38, L09602. <https://doi.org/10.1029/2011GL047174>
- Socolofsky, S. A., Bhaumik, T., & Seol, D. G. (2008). Double-plume integral models for near-field mixing in multiphase plumes. *Journal of Hydraulic Engineering*, 134(6), 772–783. [https://doi.org/10.1061/\(ASCE\)0733-9429\(2008\)134:6\(772\)](https://doi.org/10.1061/(ASCE)0733-9429(2008)134:6(772))
- Sokolichin, A., Eigenberger, G., Lapin, A., & Lübert, A. (1997). Dynamic numerical simulation of gas–liquid two-phase flows Euler/Euler versus Euler/Lagrange. *Chemical Engineering Science*, 52(4), 611–626. [https://doi.org/10.1016/S0009-2509\(96\)00425-3](https://doi.org/10.1016/S0009-2509(96)00425-3)
- Sullivan, P. P., McWilliams, J. C., & Moeng, C.-H. (1994). A subgrid-scale model for large-eddy simulation of planetary boundary-layer flows. *Boundary-Layer Meteorology*, 71(3), 247–276. <https://doi.org/10.1007/BF00713741>
- Tsuchiya, K., Mikasa, H., & Saito, T. (1997). Absorption dynamics of CO₂ bubbles in a pressurized liquid flowing downward and its simulation in seawater. *Chemical Engineering Science*, 52(21–22), 4119–4126. [https://doi.org/10.1016/S0009-2509\(97\)00254-6](https://doi.org/10.1016/S0009-2509(97)00254-6)
- Veron, F. (2015). Ocean spray. *Annual Review of Fluid Mechanics*, 47, 507–538. <https://doi.org/10.1146/annurev-fluid-010814-014651>
- Wang, B., Lai, C., & Socolofsky, S. (2019). Mean velocity, spreading and entrainment characteristics of weak bubble plumes in unstratified and stationary water. *Journal of Fluid Mechanics*, 874, 102–130. <https://doi.org/10.1017/jfm.2019.461>
- Wang, B., & Socolofsky, S. A. (2019). Characteristics of mean flow and turbulence in bubble-in-chain induced flows. *Physical Review Fluids*, 4, 54,302. <https://doi.org/10.1103/PhysRevFluids.4.054302>
- Yang, D., Chamecki, M., & Meneveau, C. (2014). Inhibition of oil plume dilution in Langmuir ocean circulation. *Geophysical Research Letters*, 41, 1632–1638. <https://doi.org/10.1002/2014GL059284>
- Yang, D., Chen, B., Chamecki, M., & Meneveau, C. (2015). Oil plumes and dispersion in Langmuir, upper-ocean turbulence: Large-eddy simulations and K-profile parameterization. *Journal of Geophysical Research: Oceans*, 120, 4729–4759. <https://doi.org/10.1002/2014JC010542>
- Yang, D., Chen, B., Socolofsky, S. A., Chamecki, M., & Meneveau, C. (2016). Large-eddy simulation and parameterization of buoyant plume dynamics in stratified flow. *Journal of Fluid Mechanics*, 794, 798–833. <https://doi.org/10.1017/jfm.2016.191>
- Yapa, P. D., Dasanayaka, L. K., Bandara, U. C., & Nakata, K. (2010). A model to simulate the transport and fate of gas and hydrates released in deepwater. *Journal of Hydraulic Research*, 48, 559–572. <https://doi.org/10.1080/00221686.2010.507010>
- Yapa, P., & Li, Z. (1997). Simulation of oil spills from underwater accidents I: Model development. *Journal of Hydraulic Research*, 35(5), 673–688. <https://doi.org/10.1080/00221689709498401>
- Yapa, P., & Zheng, L. (1997). Modelling oil and gas releases from deep water: A review. *Spill Science and Technology Bulletin*, 4(4), 189–198. [https://doi.org/10.1016/S1353-2561\(98\)00020-6](https://doi.org/10.1016/S1353-2561(98)00020-6)
- Zhao, L., Boufadel, M. C., Lee, K., King, T., Loney, N., & Geng, X. (2016a). Evolution of bubble size distribution from gas blowout in shallow water. *Journal of Geophysical Research: Oceans*, 121, 1573–1599. <https://doi.org/10.1002/2015JC011403>
- Zhao, L., Shaer, F., Robinson, B., King, T., D'Ambrose, C., Pan, Z., et al. (2016b). Underwater oil jet: Hydrodynamics and droplet size distribution. *Chemical Engineering Journal*, 299, 292–303. <https://doi.org/10.1016/j.cej.2016.04.061>
- Zheng, L., & Yapa, P. D. (2000). Buoyant velocity of spherical and nonspherical bubbles/droplets. *Journal of Hydraulic Engineering*, 126(11), 852–854. [https://doi.org/10.1061/\(ASCE\)0733-9429\(2000\)126:11\(852\)](https://doi.org/10.1061/(ASCE)0733-9429(2000)126:11(852))
- Zheng, L., & Yapa, P. D. (2002). Modeling gas dissolution in deepwater oil/gas spills. *Journal of Marine Systems*, 31(4), 299–309. [https://doi.org/10.1016/S0924-7963\(01\)00067-7](https://doi.org/10.1016/S0924-7963(01)00067-7)
- Zheng, L., Yapa, P. D., & Chen, F. (2003). A model for simulating deepwater oil and gas blowouts—Part I: Theory and model formulation. *Journal of Hydraulic Research*, 41(4), 339–351. <https://doi.org/10.1080/00221680309499980>